Statistical properties of mass, star formation, chemical content and rotational patterns in early $z \gtrsim 9$ structures

V. Biffi[1,2,3]*, U. Maio[4,5,6]†

[1] *SISSA - Scuola Internazionale Superiore di Studi Avanzati, Via Bonomea 265, 34136 Trieste, Italy*
[2] *Max-Planck-Institut für Astrophysik, Karl–Schwarzschild–Straße 1, 85748 Garching bei München, Germany*
[3] *Universidad Autónoma de Madrid, Departamento de Física Teorica, Ciudad Universitaria de Cantoblanco, 28049 Madrid, Spain*
[4] *INAF – Osservatorio Astronomico di Trieste, via Tiepolo 11, 34143 Trieste, Italy*
[5] *Max-Planck-Institut für extraterrestrische Physik, Giessenbachstraße 1, 85748 Garching bei München, Germany*
[6] *Leibniz-Institut für Astrophysik, An der Sternwarte 16, 14482 Potsdam, Germany*

6 December 2013

ABSTRACT

We study the baryonic, chemical and dynamical properties of a significantly large sample of early proto-galaxies in the first 500 Myr of the Universe (redshift $z \gtrsim 9$), obtained from high-resolution numerical, N-body, hydrodynamical, chemistry simulations including atomic and molecular networks, gas cooling, star formation, stellar evolution and metal spreading for population III and population II-I regimes according to proper stellar yields and lifetimes. We find that first star formation events take place in halos with dark-matter mass $M_{DM} > 2 \times 10^6$ $M_\odot$. Early star forming objects have: molecular fractions from $x_{mol} \lesssim 10^{-4}$ in quiescent structures up to $x_{mol} \gtrsim 0.1$ in active regions; star formation rates SFR $\sim 10^{-8} - 10^{-3}$ $M_\odot/yr$; and metallicities in the range $\sim 10^{-8} - 10^{-2}$ $Z_\odot$. Roughly $\sim 10\%$ of high-z haloes host population II-I star formation and dominate the cosmic SFR density. They usually are bursty objects with mean specific SFR around $\sim 10\,Gyr^{-1}$ at $z \sim 9$ and increasing with redshift up to $\sim 10^2\,Gyr^{-1}$. Stellar feedback effects alter the baryonic content of the haloes and locally affect their chemical and thermo-dynamical properties, as reflected by the broadening of various physical relations. The establishment of gaseous rotationally-supported cores is quite uncommon, weakly related to the large-scale dark-matter behaviour and evolving in an intermittent fashion. The colder, molecular-rich phase tends to maintain any established rotational motion longer with respect to the hotter, metal-rich component, which is very sensitive to environmental processes. While the fraction of haloes featuring a significant amount of co-rotating, molecular-rich gas increases with cosmic time (from a few per cent at $z \sim 20$ up to $\sim 5 - 15\%$ at $z \sim 9$), the chaotic nature of metal-enriched material does not lead to particular trends.

Key words: cosmology - theory: early Universe; methods - numerical simulations.

1 INTRODUCTION

Cosmological structure formation at high redshift is a particularly interesting topic, because it probes the infancy of the very first galaxies, and the chemical and thermal conditions of the early Universe.

Primordial, molecular-rich star forming regions are responsible for a variety of physical processes in the cosmic medium: they are the main sources of cosmic metal and dust enrichment with consequent transition from pristine population III (popIII) stars to standard population II-I (popII-I) stars (Tornatore et al. 2007; Maio et al. 2010, 2011; Wise

et al. 2012); are relevant sites of production of photons that reionize the Universe (Abel et al. 2002; Sokasian et al. 2004; Robertson et al. 2010; Salvaterra et al. 2011; Fernandez & Shull 2011; Petkova & Springel 2011) or dissociate molecules (Ricotti et al. 2001; Whalen et al. 2008; Petkova & Maio 2012); are supposed to be at the origins of the cosmic near infra-red background (Dwek & Arendt 1998; Gorjian et al. 2000; Totani et al. 2001; Santos et al. 2002; Magliocchetti et al. 2003; Cooray et al. 2004; Kashlinsky 2005; Kashlinsky et al. 2012; Fernandez & Zaroubi 2013); are important places for black-hole seed formation (Madau & Rees 2001; Bromm & Loeb 2003a; Alvarez et al. 2009; Johnson et al. 2012); have observational counterparts in, e.g., Lyman-break galaxies or Lyman-α emitters (Bouwens et al. 2012; Jeeson-Daniel

* E-mail: biffi@sissa.it (VB)
† maio@oats.inaf.it (UM), Marie Curie Fellow

et al. 2012); are preferential hosts of long gamma-ray bursts (GRBs) (Campisi et al. 2011; Maio et al. 2012; Salvaterra et al. 2013); reflect higher-order effects in the primordial velocity field (Tseliakhovich & Hirata 2010; Maio et al. 2011; Stacy et al. 2011; Greif et al. 2011; McQuinn & O'Leary 2012; Fialkov et al. 2012; Naoz et al. 2012, 2013; Richardson et al. 2013); and can be used as tracers of dark-matter non-Gaussianities (Maio & Iannuzzi 2011; Maio 2011a; Maio & Khochfar 2012), or even as dark-energy probes on large scales (Maio et al. 2006).

Although it is quite commonly accepted (Gunn & Gott 1972) that first star formation events take place in the growing dark-matter haloes, where gas can cool, fragment and acquire angular momentum (Toomre 1977; White & Rees 1978), there are still controversial debates about properties and degeneracies for the baryonic component in primordial mini-haloes (Bower et al. 2010). From low-redshift observations, it is rather well established that star formation activity is strictly linked to the gaseous content of cosmic structures (Schmidt 1959; Kennicutt 1998) and represents the main driver of metal pollution (Tremonti et al. 2004). Observational detections suggest the presence of early galaxies at $z \simeq 11$ (e.g. Zheng et al. 2012; Coe et al. 2013), with corresponding formation redshift $z \sim 14$ (Bouwens et al. 2012). Recent numerical works have pointed out that galaxies in the first billion years shape fairly well the observed luminosity function (Salvaterra et al. 2013). Never the less, uncertainties on the role of different feedback mechanisms on the first star formation sites, on their surrounding environments and on their local dynamical state still persist.

Despite possible connections between the dynamical features of primeval dark-matter haloes and the hosted gas (de Souza et al. 2013), *ad hoc* studies of individual cases (e.g. Stacy et al. 2013; Prieto et al. 2013) have claimed that the dynamical trends of collapsing gas can be completely decoupled from the large-scale hosting halo (i.e. the spins do not necessarily coincide). Studies on dark-matter haloes have demonstrated that the total spin of the halo is only mildly correlating with mass, whereas the correlation with substructures, local environment and halo concentration is usually stronger (see, e.g., Jeeson-Daniel et al. 2011; Skibba & Macciò 2011, where, however, disc formation in the gas component was not specifically addressed). This is somehow consistent with additional analyses showing that gaseous disc and fragmentation properties result substantially influenced by gas cooling or feedback mechanisms (e.g. Piontek & Steinmetz 2011; Moster et al. 2012; Halle & Combes 2012; Maio et al. 2013; Vogelsberger et al. 2013) and rotational patterns can experience enhancement or disruption according to the specific ambient medium (mostly at high z; Genzel et al. 2008). Moreover, the gaseous cold flows that are expected to give birth to baryonic stellar structures are invoked in literature both as responsible for the establishment of extended discs (Kereš et al. 2005; Brooks et al. 2009; Dekel et al. 2009) and as responsible of bulge growth (Sales et al. 2012). Such contrasting conclusions testify that a unique and definitive understanding of this subject has not been reached, yet.

At high z our knowledge is particularly limited, because baryonic and dynamical properties in early objects could be only recently investigated with the help of suited numerical simulations. In a few dedicated works (Wise & Abel 2007; Greif et al. 2008; Romano-Díaz et al. 2011; Stacy & Bromm

2013; Prieto et al. 2013; Xu et al. 2013) the thermodynamical state of the gas, the establishment of rotationally-supported cores and the morphologies of primordial haloes have been explored for some specific cases by means of hydrodynamical simulations including molecular cooling in pristine gas. However, additional, larger samples to draw firmer conclusions on the statistical trends at different times would be required. Further studies need to be performed to unveil the effects of stellar evolution and consequent metal spreading according to proper yields and lifetimes on structure growth and disc formation. Indeed, it is crucial to take into account hot, enriched gas ejected from type II and type Ia supernovae (SN) or during asymptotic-giant-branch (AGB) phases in the surrounding colder, molecular-rich environments to fairly assess the subsequent evolution of the surrounding gas. More in detail, it would be interesting to know what the typical baryonic properties in primordial mini-haloes are; what their metal and chemical content is and how it changes with time; which fraction of haloes can host popIII or popII-I star formation; how thermal and dynamical properties are affected by supernova esplosions or feedback mechanisms; what connections between stellar growth and local environment can be established; whether it is possible to find relations between stellar mass and chemical composition (metallicity and/or molecular fraction); if the specific star formation rate has different trends at early and late cosmological times; how primordial, molecular-rich discs can form, host star formation and survive to stellar feedback; what rotational patterns can be expected in such high-redshift structures and how different components behave from a dynamical point of view.

In this paper, we plan to address these issues by exploring both the typical features of early star forming gas and the implications for the resulting angular momentum and rotational patterns. We will use high-resolution numerical simulations focusing on the first ~ 500 Myr of the Universe and corresponding to $z \gtrsim 9$.

The work is organized as follows: in Section 2 we describe the simulations and in Section 3 we present the data set selected for the analysis. In Section 4 we discuss the main results about: baryonic – thermal and chemical – properties of primordial haloes (Section 4.1), their link to star formation activity (Section 4.2) and the evolving dynamical features of the first molecular-rich star formation sites (Section 4.3). We summarize and conclude in Section 5.

2 SIMULATIONS OF PRIMORDIAL HALOES

We consider N-body, hydrodynamical, chemistry simulations (see Maio et al. 2010, 2011; Maio & Iannuzzi 2011) in a standard ΛCDM model with geometrical parameters: $\Omega_{0,\Lambda} = 0.7$, $\Omega_{0,m} = 0.3$, $\Omega_{0,b} = 0.04$, for present-day Λ, total-matter, baryonic-matter density parameters, and expansion parameter normalized to $100 \, \mathrm{km/s/Mpc}$, $h = 0.7$. Spectral parameters are assumed to be $\sigma_8 = 0.9$, and $n = 1$, for the power spectrum normalization via mass variance within $8 \, \mathrm{Mpc}/h$−size sphere, and for the power spectrum slope, respectively. The cosmological field is sampled at redshift $z = 100$ with 2×320^3 gas and dark-matter particles in a cube of $\sim 0.5 \, \mathrm{Mpc}/h$ a side, for a resulting gas mass resolution of roughly $\sim 40 \, \mathrm{M}_\odot/h$.
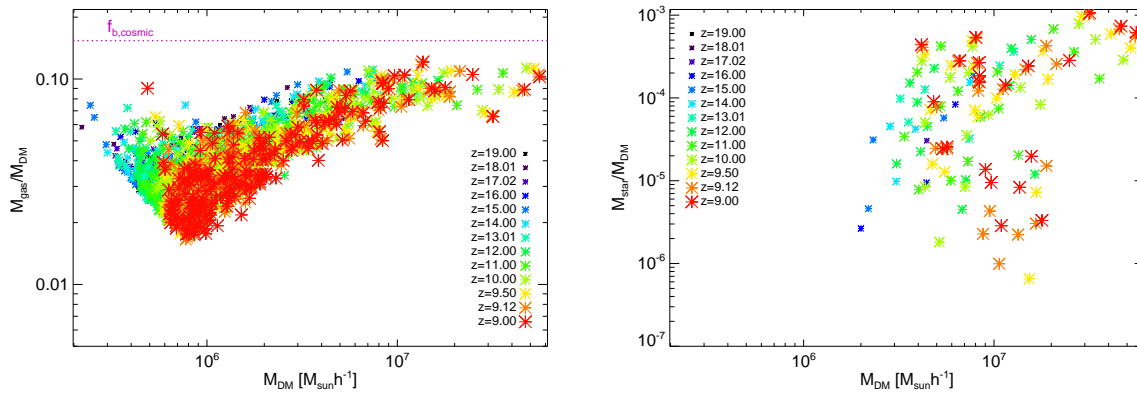
Figure 1. Relations between the gas fraction (left) and stellar fraction (right) as function of dark-matter mass, $M_{\rm DM}$ at different redshifts (see legends). The horizontal dotted line marks the cosmological baryon fraction, computed according to the simulation parameters.

The implementation includes non-equilibrium chemistry evolution for e^-, H, H^+, H^-, He, He^+, He^{++}, H_2, H_2^+, D, D^+, HD, HeH^+ (Yoshida et al. 2003; Maio et al. 2007; Petkova & Maio 2012), gas cooling from resonant, fine-structure and molecular lines (as in Maio et al. 2007), star formation, feedback (Springel & Hernquist 2003), stellar evolution and metal pollution from different stellar yields: He, C, O, Si, Fe, Mg, S, etc. (Tornatore et al. 2007, 2010). Stellar population transition with a switch on the initial mass function (IMF) takes place when a critical metallicity of $Z_{crit} = 10^{-4} Z_\odot$ is reached (Bromm & Loeb 2003b; Schneider et al. 2003): star forming regions with $Z < Z_{crit}$ (popIII) are assumed to have a top-heavy IMF in the range $100 - 500 \, M_\odot$ with a slope of -2.35, while star forming regions with $Z \geqslant Z_{crit}$ (popII-I) form stars according to a Salpeter IMF. For further details we refer the interested reader to Maio et al. (2007, 2010, 2011, 2013), and references therein. We stress that this kind of implementation permits us to properly follow detailed chemical evolution of the medium both in pristine, popIII regimes and in enriched, popII-I ones, simultaneously taking into account the changes in the local stellar populations and the consequent energetics of feedback mechanisms.

In the following we will clarify our selection criteria and show the main results about the baryonic and dynamical properties of primordial structures.

3 SELECTION AND DATA SET

We track cosmological structures with their dark-matter, gaseous, and stellar components by applying a friend-of-friend (FoF) algorithm (Dolag et al. 2009) with linking length equal to 20 per cent the mean inter-particle separation and by storing their properties (constituting particles, centers of mass, masses, positions, velocities, metal abundances, atomic and molecular fractions, star formation rates, temperatures, etc.) for each redshift.

The total number of haloes usually ranges from a few tousands at very high redshift up to several tens of tousands at later times and reaches about ~ 25000 primordial objects at $z \simeq 9$. In order to have a set of haloes whose matter components are properly resolved, at each snapshot we select only

objects with at least 300 gas particles. We notice that this constraint is quite conservative and protects us from deviations due to numerical artifacts. Indeed, artificial results would be obtained if a number of gas particles lower than 4 times the number of neighbours were employed (Bate & Burkert 1997). Since we use 32 neighbors in the density estimation, with our choice we select only objects for which no spurious fragmentation takes place. We also stress that the selection is done on the number of gas particles only, so the selected objects have a *total* number of particles that is much larger, usually of at least one order of magnitude, and results in a minimum of at least a few tousands particles. This also avoids unphysical two-body numerical heating (e.g. Vazza et al. 2011). The final data set resulting from our selection consists of 1680 haloes between $z = 9$ and $z \simeq 20$, of which about 200 at redshift $z = 9$. Gas and stellar fractions as a function of dark-matter mass are summarized in Fig. 1 for different redshifts (see discussion in the next).

We highlight that we additionally checked our results by applying different cuts in the number of gas particles in each halo (i.e. 200, 250, 300), and, then, by considering the (50, 100, 200) largest haloes in the catalogue list. However, all the resulting trends did not show evident changes and the statistical patterns were basically unaffected.

4 RESULTS

We will now show the principal features of the first galaxies at high redshift, and their baryonic and dynamical properties.

Fig. 1 shows gas (left-hand side panel) and stellar (right-hand side panel) fractions as a function of dark-matter mass, while the horizontal line marks the cosmological baryon fraction. Both gas and stellar content can vary within haloes of different dark-matter masses, M_{DM}, due to the interplay of gas cold inflows and hot ejected material. In particular, bigger haloes are able to retain the gas heated by star formation feedback, while smaller ones have shallower potential wells and can loose significant amounts of mass. This is clearly demonstrated by the large spreads for low gas masses and the deep decrement around $\sim 10^5 - 10^6 \, M_\odot$. Therefore, formation of stars in haloes with a dark mass below
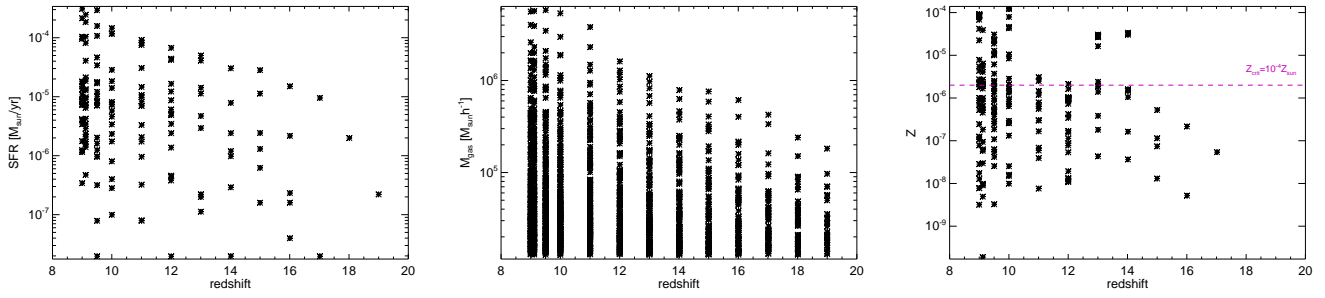
Figure 2. Redshift evolution of SFR (left), M_{gas} (center) and total metallicity Z (right) for our set of haloes. In the $redshift - Z$ panel, the purple dashed line marks the critical threshold of $Z_{\rm crit} = 10^{-4}$ $Z_\odot$.

$\sim 2 \times 10^6$ $M_\odot$ is strongly inhibited, as testified by the right panel and as also found by Wise et al. (2012). Stellar fractions are generally increasing with dark-matter mass[1] and span a range between $\sim 10^{-6}$ and 10^{-3} for hosting halo masses of $\sim 10^6 - 10^8$ $M_\odot/h$. The basic reason why there is no relevant star formation below the minimum mass of $\sim 2 \times 10^6$ $M_\odot$ lies in the relatively low densities reached by the hosted gas. As a consequence, in such small objects, H_2 and HD molecules either are not formed significantly or, in case, are not efficiently shielded, thus star formation feedback in close, more massive haloes can easily dissociate them.

In the following sections, we will analyze in detail the properties of these objects: their baryonic features (Section 4.1), the connections to star formation activity (Section 4.2) and eventually their dynamical patterns (Section 4.3).

4.1 Baryonic properties of early proto-galaxies

We start by discussing the basic physical properties of primordial popIII and popII-I galaxies (Section 4.1.1), their gas, molecule, and metal content (Section 4.1.2) and their thermal state (Section 4.1.3).

We note that, since the number of well-resolved haloes is 1680 and the structures having a non-null star formation rate (SFR > 0) are 148, the fraction of cosmological objects effectively involved in high-redshift star formation is roughly $\sim 10\%$ per cent. Pollution events from star formation episodes can influence a significant fraction of closeby regions, as 83 proto-galaxies are found to have SFR $= 0$ and $Z > 0$, while the bulk of enriched ($Z > 0$) objects consists of 206 early galaxies, i.e. about 2.5 times more.

4.1.1 PopIII and popII-I star forming galaxies

As already discussed in different works in literature (Maio et al. 2010; Maio & Iannuzzi 2011; Campisi et al. 2011; Wise et al. 2012; Salvaterra et al. 2013), the popIII contribution to the total star formation process is important only during the very initial bursts of star formation, while the bulk of cosmic star formation is usually dominated by the popII-I

---

[1] **Despite the scatter at low masses, the correlation of $M_\star/M_{DM}$ with halo mass is mildly positive, as quantified by the Pearson correlation coefficient, ~ 0.74, and by Spearman's rank correlation, ~ 0.43.**
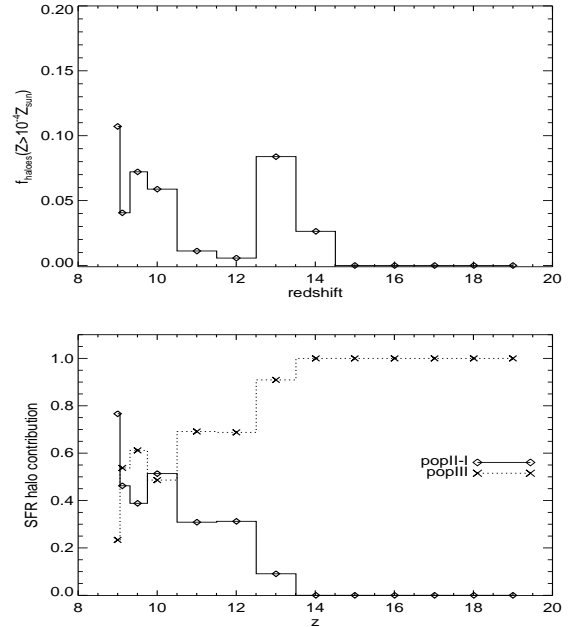

Figure 3. *Upper panel:* redshift evolution of the fraction of haloes with gas metallicity above the critical threshold of $Z_{\rm crit} = 10^{-4}$ $Z_\odot$ (popII-I haloes). *Lower panel:* Redshift evolution of the relative contribution of popII-I (solid curve) and popIII (dashed) haloes to the total SFR. **UM: l'asse x del plot in alto e' redshift, invece quello del plot in basso e' z.**

regime. Obviously, popIII star formation can still take place at later times, but only in pristine, unpolluted regions not yet affected by chemical feedback. Never the less, the most star forming regions in the Universe are expected to be already significantly enriched by redshift $z \sim 10$.

To better quantify the contribution of the haloes involved in the enrichment process and their stellar regime properties, we show, in Fig. 2, the redshift evolution of the star formation rates, gas masses, and metallicities in our set of haloes. Generally, these three quantities are increasing with time, as a consequence of the growth of the cosmic perturbations that lead star forming activity and consequent metal spreading. The objects considered here have typical gas masses of up to $\sim 10^7$ $M_\odot$ and star formation rates spanning almost 5 orders of magnitudes, from a few times 10^{-8} $M_\odot$/yr up to several times 10^{-4} $M_\odot$/yr at $z \simeq 9$. Interestingly, some
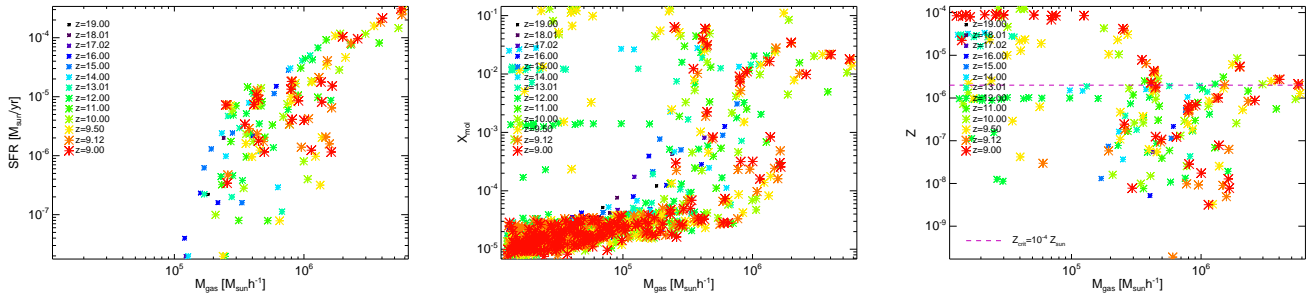
Figure 4. Relations between gas mass, M_{gas}, and star-formation rate, SFR (left), molecular fraction, x_{mol} (center), and metallicity, Z (right). Color code and symbol size are given according to redshift, as in the legends. The purple horizontal dashed line in the right panel is drawn in correspondence of the critical metallicity $Z_{\rm crit} = 10^{-4}$ $Z_\odot$.

haloes are enriched well above $Z_{\rm crit}$ already at $z \lesssim 14$.
A more quantitative result on the abundance of popIII and popII-I haloes is plotted in Fig. 3 **(upper panel)**, where we show the redshift evolution of the fraction of enriched haloes with gas metallicity above the critical threshold $Z_{\rm crit} = 10^{-4}$ $Z_\odot$. It emerges that usually only up to ~ 10 per cent of the enriched haloes have $Z > Z_{\rm crit}$. **Correspondingly, the lower panel of Fig. 3 shows the relative contribution of different-population haloes to the cosmic star formation: pristine, molecular-cooling, popIII haloes (dotted line) and enriched metal-cooling, popII-I haloes (solid line). The fraction of star formation processes hosted by popIII haloes decreases rapidly with redshift, whereas the contribution by popII-I haloes becomes more and more important. Basically, metal-rich haloes start contribute the cosmic star formation activity and metal pollution at $z \lesssim 14$ and dominate it below $z \sim 10$.** The **initial** rapid increment in Z is a consequence of efficient spreading from the first star forming regions. The effects of metal pollution are particularly stronger at earlier times, because of the more powerful and energetic feedback from primordial popIII sources. This causes the peak **of popII-I structures** at $z \sim 13$ **(upper panel) with consequent onset of metal-driven star formation (lower panel)** [2]. The non-very-regular trend in **the upper panel of** Fig. 3, is due both to metals escaping from the haloes, and to occurring merging events with low-metallicity objects or pristine gas that can dilute metallicities.
UM:
We also note that Fig. 3 supports the possibility of forming substantial amounts of popIII galaxies at relatively lower redshift, altough passively evolving.

4.1.2 Chemical properties of the first galaxies

In Fig. 4, we plot the dependencies of star formation rate (left panel), molecular fraction (central panel), and metallicity (right panel) from the gas mass of the various objects. The relation between star formation rate and gas mass results roughly linear, despite a wider spread at low masses, and consistent with Fig. 1 (right panel).

---

[2] We remind that among all the $Z > 0$ haloes (206) between $z \sim 9$ and $z \sim 20$ about 40 per cent (83) have null SFR.

In such regimes, proto-galaxies are experiencing the very first bursts of star formation (with a rapidly increasing star formation rate), but have not necessarily formed stars, yet. In the whole redshift range considered, the smaller proto-galaxies ($\sim 10^5 - 10^6$ $M_\odot/h$ in gas) that are just undergoing their first bursts (SFR > 0, but $M_\star = 0$) correspond to roughly ~ 20 per cent of the total (27 objects out of 148) star forming objects, while the remaining ~ 80 per cent (121 out of 148) has already experienced star formation and feedback effects (SFR > 0 and $M_\star > 0$). Thus, the spread at the low-mass end simply reflects these initial star formation stages, in contrast to those structures that have already an established star formation activity and lie on the roughly linear correlation individuated by the upper envelope of the distribution. The general trend and the residual spread can be attributed to the competitive effects of different feedback mechanisms: on one hand, the gas undergoing star formation is heated by SN explosions and inhibited to continue forming stars, mostly in smaller structures that suffer significantly gas evaporation processes (negative feedback); on the other hand, shock compressions and spreading of metals in the medium enhance gas cooling capabilities and induce more star formation (positive feedback), mostly in bigger objects that can trap and re-process larger amounts of material. The sensitivity to feedback is also well visible by comparing the trend of e.g. $z \sim 16 - 17$ (blue) points below $\sim 10^6$ $M_\odot/h$, that are quite aligned with the upper envelope of the dispersion plot and have not experienced feedback mechanisms, yet, and the corresponding (green) points at $z \sim 10 - 11$, in the same mass range, that are much more scattered due to the ongoing feedback effects in the local environments.
When looking at the cold molecular gas in the different objects at various redshifts (central panel), we find that molecular fractions, x_{mol}, are rather low ($x_{mol} < 10^{-4}$) mostly in small, quiescent, objects that are not star forming, like many of those with a gas mass $\lesssim 10^5$ $M_\odot$. These galaxies populate significantly the bottom-left part of the diagram, where the corresponding star formation rates plotted on the left panel are null. The regular trend of increasing molecular fraction with increasing mass is visible up to $z \sim 15 - 16$, when initial collapse phases boost x_{mol} up to $\gtrsim 10^{-3}$, in galaxies of $\sim 10^5 - 10^6$ $M_\odot$, that are forming their first stars and are not altered by feedback mechanisms. At $z \lesssim 15$, feedback effects from the first star forming galaxies become responsible for dispersing the values of molecular fractions of several orders of magnitude, either by dissociating molecules (hence,

lowering their fraction), or by partially enhancing their formation (hence, increasing their fraction) by shocks and gas compression (e.g. Ricotti et al. 2001; Whalen et al. 2008; Petkova & Maio 2012). For these reasons, molecular fractions in larger structures at later times have a scatter of a few orders of magnitudes, and some small mini-haloes have a somewhat more sustained molecular content at $z \sim 14 - 10$. However, the total amount of cold gas in such small protogalaxies is not enough to induce significant star formation episodes.

Investigating the gas metallicity evolution in haloes of different mass (right panel) is useful to have hints about metal enrichment and to distinguish structures enriched by internal sources by those enriched by external ones. Of course, we do not find points corresponding to low-mass and high-redshift haloes, where in fact there is only pristine, not enriched gas. Gas starts to be enriched by metals at $z \sim 15 - 16$, (after the first bursts of star formation), when metallicities are initially $Z \sim 10^{-8} - 10^{-7}$ (i.e., $Z \sim 10^{-6} - 10^{-5}$ $Z_\odot$), and get enhanced up to higher values at lower redshift (see also Fig. 2 and Fig. 3). A comparison among the three panels of Fig. 4 suggests that many low-mass galaxies with substantial enrichment (up to $Z \sim 10^{-4}$) at $z \lesssim 12$ have very low molecular fractions and no significant star formation: they have been basically polluted by huge amounts of hot metals ejected by SN explosions or winds located in larger, closeby star forming haloes. In particular, such enrichment process by external sources involves all the objects less massive than $\sim 10^5$ $M_\odot$ in gas, while larger ones can partially retain metals produced *in loco* and be self-enriched.

As a practical example, in the $M_{gas} - Z$ space, the (leftmost red point) halo at $z = 9$ with the smallest mass ($M_{gas} = 1.25 \times 10^5$ $M_\odot/h$), the highest metallicity ($Z = 8.46802 \times 10^{-5} \simeq 0.004$ $Z_\odot$), but very small molecular fraction ($x_{mol} = 2.49226 \times 10^{-5}$) has null star formation rate. By tracing back its evolution, it comes out that the hosting halo has formed around $z \simeq 10$ and never underwent star formation episodes and consequent self-enrichment, since molecular fractions were to low to cool down the gas and trigger collapse and fragmentation. This is actually a quiescent halo, formed in a pristine environment, and eventually enriched by hot metals coming from external sources (see next section).

4.1.3 Thermal properties of the first galaxies

Fig. 5 displays the mass-weighted gas temperatures, T_m, as a function of mass for the various redshifts considered. As gas evolution is mainly led by molecular gas, typical temperatures fall in the range $\sim 500 - 10^4$ K, where H_2 shapes the thermal conditions of early objects. Hotter temperatures are due to the thermal effects of SN explosions, whose shocks propagate in the primordial IGM, heat and enrich (see previous discussion) the gas in smaller objects (with masses $\lesssim 10^5$ $M_\odot$) – usually located within hundreds of parsecs (e.g. Creasey et al. 2012). The mass-weighted temperature increases with mass as a consequence of the virialization process in each halo, even though, the cold innermost regions will still be able to condense, collapse and fragment.

In Fig. 6, the basic relations of T_m with star formation rate (left panel), molecular fraction (central panel), and metallicity (right panel) are presented. It is interesting to stress that star formation is particularly enhanced in the $\sim 10^3 - 10^4$ K
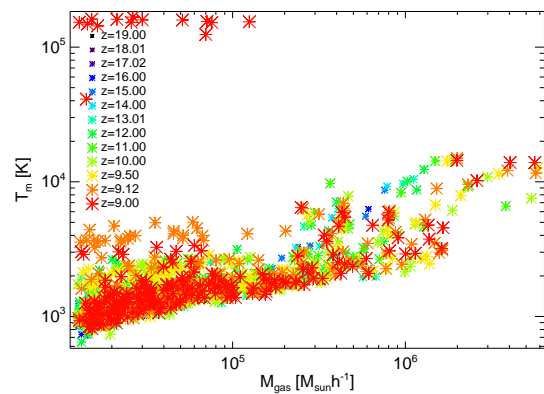

Figure 5. Relation between the gas masses, M_{gas}, and gas mass-weighted temperature, T_m. Color code and symbol size are given according to redshift, as in the legend.

regime, where molecular (H_2) cooling is mostly efficient and can determine gas collapse and fragmentation. This underlines the importance of properly following chemistry evolution to address primordial structure formation at protogalactic levels (in H_2-cooling haloes). Molecular and metallicity distributions better highlight:

• the actively star forming objects led by molecular-rich gas collapse at $T_m \sim 10^3 - 10^4$ K (central panel) and responsible for metal spreading at $z \lesssim 17$ (right panel);

• the many low-temperature, low-molecular-fraction ($x_{mol} \lesssim 10^{-4}$), pristine, quiescent objects (bottom left in the central panel, absent in the rigth panel);

• some small (see Fig. 5), high-temperature objects, whose properties are contaminated by hot enriched material at $T_m \gtrsim 10^5$ K (upper right corner in the right panel) that enhances molecule dissociation in the local gas (bottom right corner in the central panel).

These objects (14, with metallicity $Z > 10^{-4}$ $Z_\odot$) are all affected by thermal feedback processes, but particularly smaller structures (i.e. those with a gas mass $\lesssim 2 \times 10^5$ $M_\odot$) tend to be fully dominated by metal enrichment from external sources, due to the lack of significant local star formation (SFR = 0) (see also discussion about Fig. 1 and Fig. 4). Roughly speaking, they represent ~ 1 per cent of the whole sample at $z \gtrsim 9$ and correspond to ~ 7 per cent of the enriched haloes. This means that ~ 93 per cent of polluted structures are completely or partially self-enriched and, therefore, self-enrichment is a significant pollution mechanisms of cosmic haloes. Finally, when considering only passive, non-star-forming haloes (83) it turns out that purely externally enriched account for about 17 per cent of the passive population.

A summary of early objects with given physical and/or chemical properties is presented in Table 1.

4.2 Star formation and stellar activity

In the following we extend our investigations by
UM:
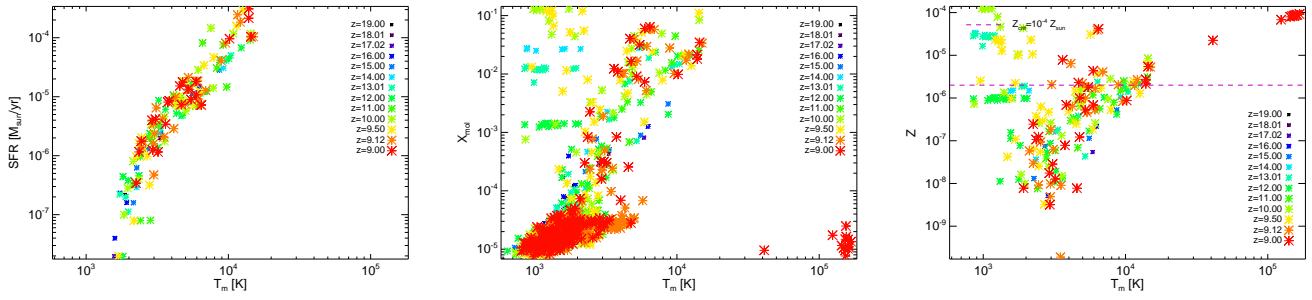**presenting the stellar features of haloes with dif-**

Figure 6. Relations between the gas mass-weighted temperature, T_m, and star formation rate, SFR (left), molecular fraction, x_{mol} (center), and total metallicity, Z (right). Color code and symbol size are given according to redshift, as in the legend. The purple horizontal dashed line in the right panel is drawn in correspondence of the critical metallicity $Z_{crit} = 10^{-4}$ $Z_\odot$.

Table 1. Number of early haloes with given properties, classified in terms of: star formation rate (SFR), molecular fraction (x_{mol}), stellar mass ($M_\star$), metallicity (Z). The total number of considered objects is 1680.

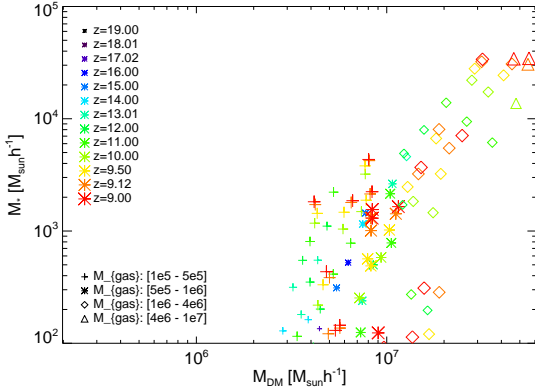|	SFR > 0	SFR $= 0$	SFR $= 0$ $x_{mol} < 10^{-4}$
$M_\star = 0$	27	1532	1470
$M_\star > 0$	121	0	0
$Z = 0$	25	1449	1449
$Z > 0$	123	83	21
$Z > 10^{-4}$ $Z_\odot$	26	47	14

Figure 7. Stellar mass as a function of dark-matter mass for the whole halo sample. Different symbols refer to different gas-mass bins: $[1 \times 10^5, 5 \times 10^5]$ M$_\odot$ (crosses), $[5 \times 10^5, 1 \times 10^6]$ M$_\odot$ (asteriscs), $[1 \times 10^6, 4 \times 10^6]$ M$_\odot$ (diamonds), $[4 \times 10^6, 1 \times 10^7]$ M$_\odot$ (triangles), as indicated by the legend on the bottom left.

ferent dark and gaseous content (Section 4.2.1), by exploring the backreaction from star formation and stellar activity (Section 4.2.2) and **by addressing** the physical relations with mass, metallicity and molecular content of star forming sites (Section 4.2.3).
UM:
We conclude the section by discussing connections between theory and data (Section 4.2.4).

4.2.1 Gas-to-star conversion efficiency

UM:
In the previous panels of Fig. 1 we have checked that larger dark-matter potential wells can retain larger amounts of gas and, hence, host more star formation. The increase of the SFR with gas mass, as shown by e.g. Fig. 4, is obviously consistent with the fact that, if more gas is available, then higher SFRs and larger stellar masses are expected. However, from our previous discussions it is still unclear whether the conversion of gas into stars will take place with the same *efficiency* or whether it will feature environmental dependencies.
To this end, we combine the information about the dark, the gaseous and the stellar components and display in Fig. 7 the trend of dark-matter mass versus stellar mass at given gas masses. From the plot, it emerges that structures with the same M_{DM} and M_{gas} usually have very variable stellar masses. Indeed, in the gas-mass bin $[1 \times 10^5, 5 \times 10^5]$ M$_\odot$ (crosses), the spread in $M_\star$ is in excess of one dex, and this holds for the $[5 \times 10^5, 1 \times 10^6]$ M$_\odot$ (asteriscs) bin, as well. For larger gas masses, as in the range $[1 \times 10^6, 4 \times 10^6]$ M$_\odot$ (diamonds), expected values for the stellar component have a scatter of more than two orders of magnitude. The most gas-rich objects, ranging within $[4 \times 10^6, 1 \times 10^7]$ M$_\odot$ (triangles), show a 'smaller' scatter, of a factor of a few, only because of statistical limitations.
For any fixed gas mass, haloes with very high stellar masses have likely experienced significant boosts by merging events. In these cases, the role of their potential wells, mainly shaped by the dark component, has been remarkable. On the other hand, more common haloes with intermediate or low stellar fractions have either evolved in isolation or their stellar growth has been (partially) suppressed by feedback mechanisms (see next section).
Overall, this means that stellar-mass formation from gas collapse (a process which is commonly parameterized by means of a gas-to-star conversion efficiency) is very strongly dependent on the particular environments and on the local ongoing physical processes. Indeed, Fig. 7 suggests that same amounts of gas mass can generate very different amounts
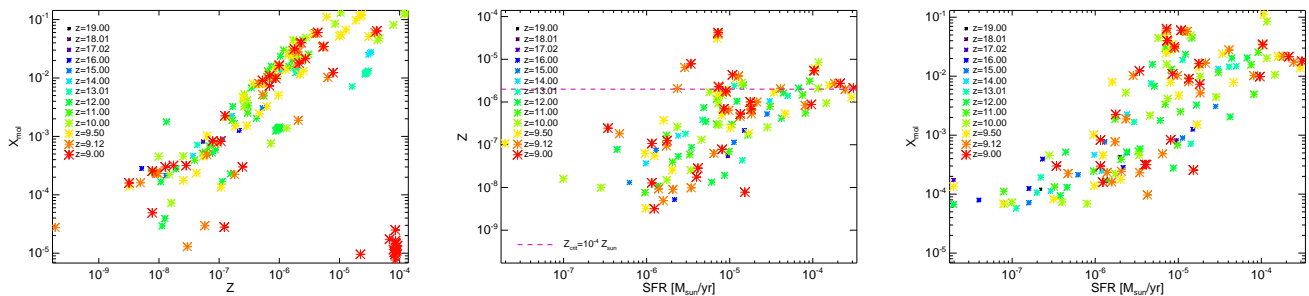
Figure 8. Relations between chemical properties and star formation. We plot the behaviour of molecular fraction, x_{mol}, and metallicity, Z (left), metallicity and star formation rate, SFR (center), and molecular fraction, x_{mol}, and star formation rate, SFR (right). Color code and symbol size are given according to redshift, as in the legend. The purple horizontal dashed line in the central panel is drawn in correspondence of the critical metallicity $Z_{crit} = 10^{-4} \ Z_\odot$.

of stellar mass, depending on, e.g., host molecular content, heavy-element abundances, cooling capabilities, SN heating, shocks, star formation feeback, gas evacuation, photoevaporation, stripping, boosting by mergers, etc.. Interestingly, this conclusion is quite independent from the particular redshift considered.

4.2.2 Effects from feedback mechanisms

Fig. 8 explicitly highlights the connections between the gaseous chemical properties of proto-galaxies (i.e. molecules and metals) and their star formation activity.

Molecule and metal distribution at different redshifts is plotted on the left panel for all the enriched galaxies in our sample. Since metals are expected to be produced by short-lived stars in molecular-rich star forming sites, the larger the molecular fractions, the larger the metallicities. A more interesting feature is the bottom right part, though: there the aforementioned objects with high metallicities and very low molecular fractions are placed. They are strongly displaced by the general trend, but this allows us to recognize the effects of metal enrichment of quiescent galaxies polluted by external sources. The upper left corner is not populated because gas with large molecular fractions of $x_{mol} \sim 10^{-2}$ or higher would have very short cooling times, hence would form immediately stars polluting the surrounding medium[3]. Consequently, the bigger the deviation from the general increasing trend, the higher the effects of feedback mechanisms. This is the case for the already mentioned smaller galaxies, while the larger ones, dominated by self-enrichment and not heavily affected by external enrichment, lie along the main trend for x_{mol} and Z.

In line with these conclusions, the central plot of Fig. 8 shows the rather weak correlation between star formation rate and gas-phase metallicity. Broadly speaking, there is an obvious tendency to have more enrichment for higher star formation rates, with the $\sim 10\%$ massive popII-I structures (see Section 4.1.1) forming stars at rates $\gtrsim 10^{-5} - 10^{-4}$ M$_\odot$/yr. However, feedback effects (more powerful for larger star formation rates) introduce a remarkable scatter that can be

noted mostly at later times (i.e. $z \lesssim 10$), when such processes are at more advanced stages and additional metals have been ejected into a wider range of star forming environments.

In addition, star formation feedback has further effects on molecular evolution (right panel). Even though molecular fractions follow more tightly star formation rates (mostly at early epochs, at $z \gtrsim 15$), the imprints of stellar evolution become visible later on, as they influence directly the thermodynamical properties of the ambient gas and hence the following formation or destruction of molecules within ~ 2 orders of magnitude.

As a conclusion, feedback effects leave prominent traces in the baryonic growth of cosmological structures that are reflected in broader and more scattered trends at later times. Natural implications are that they can easily contaminate large-scale cosmological signatures, can be relevant sources of patchiness of cosmic chemical enrichment, can alter the gas thermal state at high z, and can affect the consequent HI or molecular emissions during the late dark ages.

4.2.3 Relations between stellar and chemical properties

At this point, we study possible relations between stellar and chemical features in primordial environments.

In Fig. 9 we plot the principal stellar properties for each object at each redshift. Left panel displays the distribution of masses for gas and star component. Although the stellar content is generally larger in objects with larger amounts of gas, it is not conceivable as a fixed stellar fraction parameter, $f_\star$, simply scaling with gas or dark-matter mass. This because stars are expected to form in cold, dense, molecular-rich, collapsing gas, that is very sensitive to the typical, local environment. The broadly increasing stellar content in objects with larger gas mass is related to the fact that bigger structures have a larger probability of hosting cold molecular gas and of forming stars. On the other hand, feedback effects can (depending on the particular star formation regime, stellar evolution stages, SN rates, SFRs, halo interactions or mergers, etc.) inhibit or enhance stellar mass growth in very different ways, even in galaxies with comparable mass, causing the large spread in the data. The mass-metallicity relation (e.g. Tremonti et al. 2004) in the central panel shows a much more clear trend that is understood in terms of more metal enrichment in larger and more stellar-rich structures. Also

---

[3] This means that the probability of finding objects with $Z \simeq 0$ and $x_{mol} \sim 1$ is extremely low.
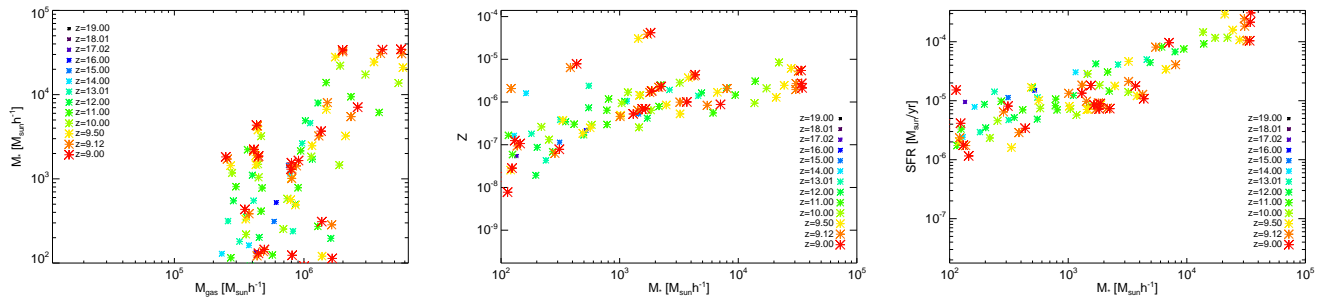
Figure 9. Relations between the stellar mass, $M_\star$, and gas mass, M_{gas}, (left), metallicity, Z (center), and star formation rate, SFR (right). Isolated Z values scattered around the bulk of the sample refer to structures subject to strong feedback and pollution processes.
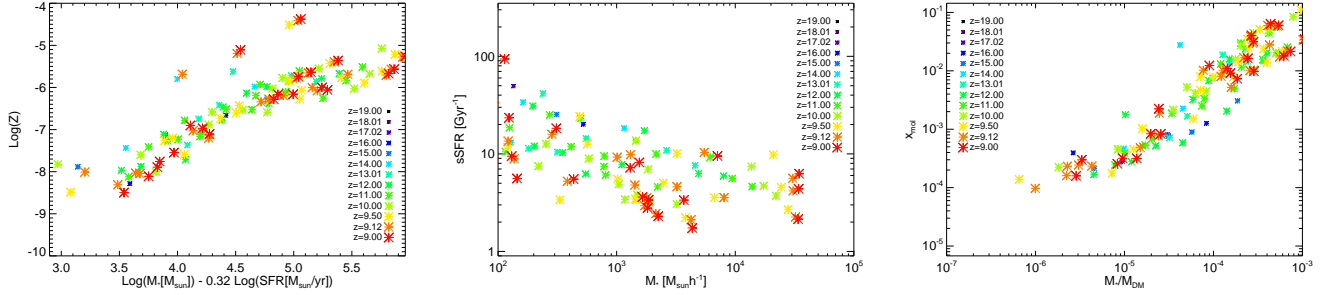

Figure 10. $SFR - M_\star - Z$ relation for our sample (left), discussed in the text. The relations $sSFR$-$M_\star$ (center) and $x_{mol} - f_\star$ (right) are also plotted for different redshifts.

in this case the outliers in the mass-metallicity relation are small structures subject to strong feedback and metal enrichment from larger, closeby sources. We note that the SFR is roughly proportional to $M_\star$, as demonstrated by the right panel, and this is consistent with local-Universe (e.g. Brinchmann et al. 2004; Salim et al. 2007; Peng et al. 2010) and intermediate-redshift (e.g. Noeske et al. 2007; Elbaz et al. 2007; Pannella et al. 2009; Rodighiero et al. 2011; Karim et al. 2011; Michałowski et al. 2010) data[4].

The left panel of Fig. 10 summarizes the various dependencies with the help of a fit-constructed relation between metallicity, star formation rate and stellar mass, containing a free parameter, α, tuned to minimize the scatter of Z. More exactly, we plot Z as a function of the adimensional combination $\mu_\alpha \equiv \mathrm{Log}(M_\star[\,M_\odot]) - \alpha \mathrm{Log}(SFR[\,M_\odot/yr])$, with $\alpha = 0.32$ fixed by fitting observational SDSS data for field galaxies at low redshift (Mannucci et al. 2010). We note that the existence of the relation between Z and $M_\star$, and the one between $M_\star$ and SFR (plotted in Fig. 9) would suggest by its-self a correlation between Z and μ_α (a function of $M_\star$ and SFR with an additional free parameter). A more limited spread for Z is obtained by tuning α. Our simulated sample shows a correlation even for early $z > 9$ proto-galaxies in primordial mini-haloes[5], even though a few outliers show up. Indeed, some points have Z values that lie significantly

away from the bulk of the sample, almost 2 orders of magnitude (as in Fig. 9). This is essentially due to feedback and pollution processes that are not properly accounted for by the μ_α parameterization (since this relies on field galaxies only) and those can determine an evident spread of the data mostly in crowded regions. It is worth stressing that, while the μ_α parameterization might be a simple and observationally friendly way to fit data, more significative physical hints can be drawn by the following equivalent expression:

$$\mu_\alpha = (1 - \alpha)\,\mathrm{Log}(SFR[\,M_\odot/yr]) - \,\mathrm{Log}(sSFR[yr^{-1}]), \quad (1)$$

where $sSFR \equiv SFR/M_\star$ is the specific star formation rate which, due to the $SFR - M_\star$ relation of Fig. 9, correlates with stellar mass (central panel of Fig. 10), as well[6]. For any fixed mass bin, the $sSFR$ features a larger spread with decreasing redshift, that appears as a consequence of the different environmental conditions developing during gas assembly and star formation episodes. Larger $sSFRs$ are typical for objects that are just forming their first stars, while smaller $sSFRs$ are found in objects that have already consumed gas available for star formation and/or have experienced the backreaction from stellar evolution.

A deeper insight into the star formation process is retrieved by means of the right panel in Fig. 10, where the molecular content of each object is plotted against its **stellar fraction, $f_\star$**. The increasing behaviour of x_{mol} for growing **stellar component** shows how tightly star formation

---

[4] We remind that observational data and stellar-mass reconstructions between $z \sim 0$ and $z \sim 3$ suggest a slope of $\sim 0.6 - 1$ and a normalization evolving with $(1+z)^{3.5}$ (see references in the text).
[5] This is in line with intermediate-redshift studies (Salvaterra et al. 2013) that reach similar conclusions for $z \sim 6 - 10$ galaxies.

[6] The correlation has a negative power, as also expected from lower-redshift observations (e.g. Daddi et al. 2007; Rodighiero et al. 2011).
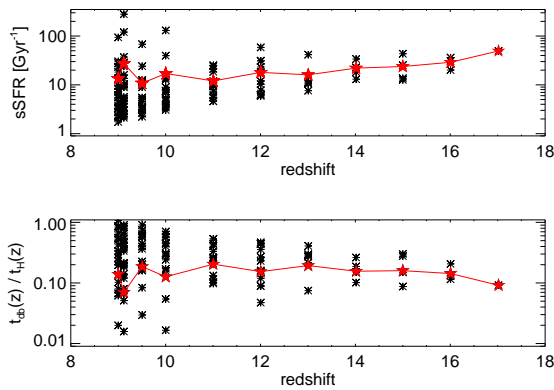
Figure 11. *Upper panel*: Redshift evolution of the specific star formation rate (sSFR) in Gyr^{-1}. *Lower panel*: Redshift evolution of the ratio between the inverse of the specific star formation rate (doubling time) and the age of the Universe (Hubble time), t_H. The solid lines connect the average values (five-points stars) at each redshift.

is linked to the chemical features of the collapsing medium. From these considerations, molecular content results to be the main driver of **stellar** growth, with an approximate scaling

$$f_\star \propto x_{mol}. \qquad (2)$$

In addition, this connotes Z as strongly related to the ongoing star formation activity, i.e. SFR and sSFR, that are in turn driven by cooling and fragmentation processes in dense, cold, molecular-rich gas.

Finally, we also plot the redshift evolution of the specific star formation rates (sSFR) in the upper panel of Fig. 11, and the corresponding evolution of the doubling times, $t_{db} = (sSFR)^{-1}$, in units of cosmic time, t_H, in the lower panel, with their respective average values (solid lines). The typical sSFR ranges between a few Gyr^{-1} and some tens of Gyr^{-1}, with some very bursty objects reaching $\sim 10^2 \, Gyr^{-1}$. Despite the evolution of the sSFR, the mean ratio between the doubling time and the corresponding Hubble time is always roughly constant in redshift, and equals: $t_{db}(z)/t_H(z) \simeq 0.1 - 0.2$, in very good agreement with later-time expectations.

4.2.4 Theory and data

We stress that the sSFR values are larger than law- or intermediate-redshift galaxies having typical sSFR $\lesssim 0.3 \, Gyr^{-1}$ at $z \lesssim 0.5$ (Noeske et al. 2007), steeply increasing to sSFR $\sim 2 \, Gyr^{-1}$ at $z \gtrsim 2$ (e.g. Daddi et al. 2007; Pannella et al. 2009; Michałowski et al. 2010; Reddy et al. 2012) and reaching sSFR $\sim 2 - 10 \, Gyr^{-1}$ at $z \sim 4 - 8$ (González et al. 2012; Stark et al. 2013). Additionally, our findings are consistent with theoretical analyses of star forming objects at $z \sim 6 - 10$ (Salvaterra et al. 2013) that suggest sSFR $\sim 10 \, Gyr^{-1}$, and are in line with recent observational estimates at $z \simeq 9.6$ (Zheng et al. 2012) and $z \sim 10.6$ (Coe et al. 2013, their Sect. 7), as well, as summarized in Fig. 12. **UM:**
We notice that theoretical calculations are fairly

comparable with data only at intermediate redshift, around $z \sim 5 - 9$. In those regimes, Salvaterra et al. (2013) could reproduce – with the help of simulations similar to the ones used here – the observed UV luminosity functions in the $[-22, -16]$ magnitude range by galaxies with stellar masses $\sim 10^4 - 10^9 \, M_\odot$, and could estimate typical SFRs (around $\sim 10^{-3} - 30 \, M_\odot/yr$) and metallicities ($\sim 10^{-3} - 10^{-1} \, Z_\odot$) for high-$z$ GRB hosts. The expected values resulted to be consistent with recent observational constraints (for details, see Salvaterra et al. 2013, and references therein). Dayal et al. (2013) reached reasonable agreement between the expected stellar mass density and corresponding values inferred observationally by e.g. Stark et al. (2013); Labbé et al. (2010). Similarly, Dunlop et al. (2013) compared their observed UV slope $\beta \simeq -2$ at $z \simeq 7 - 9$ with predictions by models of galaxy formation within cosmological chemical evolution simulations (Maio et al. 2010; Dayal et al. 2013) and found consistent results. Very recently, theoretical predictions by Maio et al. (2013) have demonstrated that cold collapsing gas or damped Ly-α candidates might be hosted already at $z \simeq 7$ in molecular-rich objects with gas masses $\sim 10^8 \, M_\odot$ and metallicities spanning several orders of magnitudes. At $z \lesssim 5$, when objects are usually bigger by a few orders of magnitude, there are discrepancies appearing between theory and data. Models seem to be roughly consistent only down to $z \sim 3$, while they fail to address star formation and stellar mass growth in massive galaxies at $z < 3$, as found by e.g. Davé et al. (2011) and Tescari (2014, private communication). On the other extreme, observational data at $z > 9$ are highly complicated to obtain. Stellar masses and SFRs for the $z = 9.6$ and $z = 10.6$ candidates in Fig. 11 were inferred by SED fitting coupled to synthetic stellar population modeling or to order-of-magnitude estimates (Zheng et al. 2012; Coe et al. 2013), for low-luminosity, strongly lensed images. Considering the large number of unknowns, degeneracies and assumptions, the resulting values carry relevant uncertainties and, therefore, it is not easy to directly confront them with our analysis. Never the less, the typical picture emerging from Fig. 12 is that the primordial Universe was made of early small galaxies that were extremely bursty, with typical sSFR $\gtrsim 50 \, Gyr^{-1}$ at $z \sim 10 - 20$, decreasing down to sSFR $\sim 10 \, Gyr^{-1}$ at $z \lesssim 10$, and sSFR $< 1 \, Gyr^{-1}$ at $z < 1$. Consistently, also metal pollution possibly led to an increase (by several orders of magnitude over cosmological time) of the typical galactic metallicities and of the expected cosmic metal filling factor (see also Maio & Iannuzzi 2011; Maio 2011b; Maio et al. 2013).

4.3 Dynamical patterns in the first structures

As a final task, we focus on the dynamical patterns of gas and dark matter components and study the trends for angular momentum calculations (Section 4.3.1). After showing a few explicative cases (Section 4.3.2), we will address the role of structure evolution in the formation and/or destruction
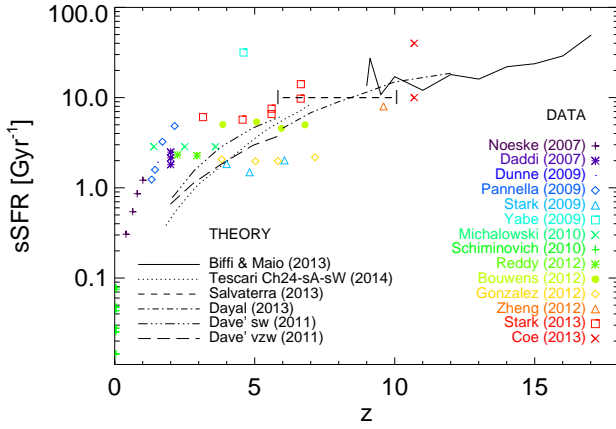
Figure 12. Redshift evolution of the specific SFR as inferred from different observational data samples and various numerical hydrodynamical simulations including gas cooling, star formation and feedback effects (see legends). The horizontal dotted line at sSFR $\simeq 10\,\mathrm{Gyr}^{-1}$ is the mean value at $z \sim 6 - 10$ expected by Salvaterra et al. (2013). The two points at $z \simeq 10.6$ are rough estimates for a stronlgy lensed image by Coe et al (2013).

of primordial gaseous discs (Section 4.3.3) and in shaping their statistical rotational features (Section 4.3.4). Then, we will check possible correlations between molecular discs and hosting masses (Section 4.3.5) and eventually the occurrence of gas and dark-matter alignment (Section 4.3.6) in primordial epochs.

4.3.1 Angular momentum calculations

Taking advantage of the full information accessible through our numerical simulations, we are able to calculate the angular momentum of any particle in the haloes. This is done by using the three-dimensional velocity associated to the particle, its distance from the halo center and its mass. Then, as usually defined (see, e.g., Binney & Tremaine 2008), the specific angular momentum, $\vec{j}$, of each particle is calculated as

$$\vec{j} = \vec{l}/m = \vec{r} \times \vec{v}, \tag{3}$$

where $\vec{l}$ is the angular momentum, $\vec{r}$ and $\vec{v}$ are the position and velocity of the particle with respect to the center, and m the particle mass.

In order to quantify the fraction of gas that might be found in rotating configurations, we calculate the mean angular momentum of the gas, $\vec{J}_{mean}$, and we compare against the specific angular momentum of each gas element, considering the projection, j_z, along the direction defined by $\vec{J}_{mean}$. Namely, the quantity

$$\eta = j_z/|\vec{J}_{mean}| \tag{4}$$

provides a measure of the alignment of the angular momentum of every single gas element with the mean angular momentum.

Alternatively, this alignment can be quantified by the cosine of the angle defined by $\vec{J}_{mean}$ and the angular momentum

of the gas element, i.e.:

$$\cos\vartheta = \frac{\vec{j} \cdot \vec{J}_{mean}}{|\vec{j}||\vec{J}_{mean}|}. \tag{5}$$

We note that, with the definition in equation (4), the value of η is not necessarily belonging to the range $[-1, 1]$, while the cosine defined in equation (5) is always in the range $[-1, 1]$.

To retrieve more information closely related to the circularity of the orbits, we calculate the commonly used quantity

$$\varepsilon = j_z/j_{circ}, \tag{6}$$

where j_z is the aforementioned component of the particle angular momentum along the direction of $\vec{J}_{mean}$ and j_{circ} is the specific angular momentum expected for a circular orbit at the same radial distance of the particle[7]. We stress that, if the particle is not bound to the halo but rather on an escaping or in-falling orbit (e.g. recently accreted), then $\varepsilon = j_z/j_{circ}$ can exceed unity. We do not exclude explicitly such not-bound particles from the calculation, nor impose the requirement that $|\varepsilon| \leqslant 1$ (see also Section 4.3.3).

Given the definition, ε is very sensitive to actual rotational orbits of the gas, so that values comprised between 0.5 and 1 (-1 and -0.5) more likely indicate co-rotating (contra-rotating) substructures in the velocity field of the gas.

Combining the information provided by both η (or equivalently $\cos\vartheta$) and ε, one can put tighter constraints on the presence of actual, ordered, rotational patterns in the gas for all the 1680 haloes between $z = 9$ and $z \simeq 20$ in our sample.

To study the trends of the different gas components, the calculations are also done for the molecular and metal-rich gas phases separately. Specifically, we focus on:

- *molecular-rich* gas with $x_{mol} > 5 \times 10^{-4}$.
- *metal-rich* gas with metallicity $Z > 10^{-3}\ \mathrm{Z}_\odot$;
- *metal-rich* gas with metallicity $Z > 10^{-4}\ \mathrm{Z}_\odot$.

4.3.2 Rotational patterns: representative cases

In Fig. 13 a few haloes with different masses are chosen to represent possible dynamical configurations. The spatial maps in the two projections give a visual impression of the gas structures in the halo central part, i.e. within 0.5 kpc/h comoving radius[8] (numerical studies and converges are discussed in Appendix A). Points in the maps are color-coded according to the gas phase, i.e. red for molecular-rich gas, green for metal-rich gas with metallicity $Z > 10^{-3}\ \mathrm{Z}_\odot$ and blue for metal-rich gas with metallicity $Z > 10^{-4}\ \mathrm{Z}_\odot$. Black points refer to all the gas particles in the plotted region. The same color-code is applied to the distributions shown in the third and fourth columns. For comparison, we overplot the η distribution for all the gas in the selected region

---

[7] We use

$$j_{circ} = rv_{circ}(r), \tag{7}$$

where r is the radial distance of the particle with respect to the halo center, and $v_{circ}(r) = \sqrt{GM(r)/r}$ in spherical symmetry.

[8] We consider a typical region of 0.5 kpc/h comoving radius, which, for proto-galaxies at such high redshifts ($9 \lesssim z \lesssim 20$) represents a significant fraction of the virial radius.
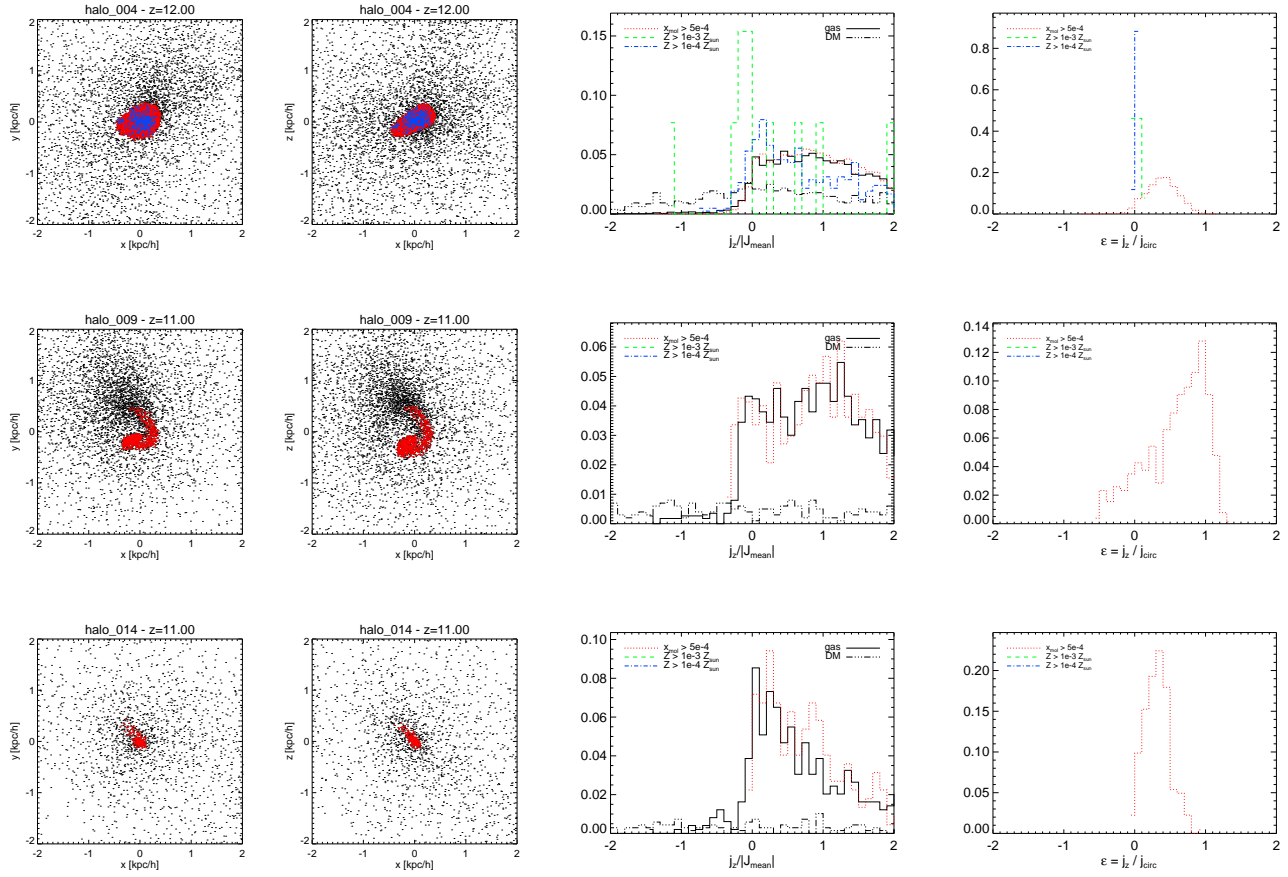
Figure 13. Representative haloes at redshift $z \sim 12$ (top row) and $z \sim 11$ (middle and bottom rows), when the Universe was 0.361 Gyr and 0.407 Gyr old, respectively. The three haloes show a variety of configurations, including both elongated molecular structures built in the contraction process of isolated haloes, and tail-like features where the rotational motion of the gas is clearly driven by environmental interactions (e.g. the in-falling and merging with a sub-halo.). *First and second column*: spatial distribution of the gas in the xy and xz planes, respectively; different colours refer to the different gaseous components: all the gas (black points), molecular-rich gas with $x_{mol} > 5 \times 10^{-4}$ (red points), metal-rich gas with $Z > 10^{-3}\,Z_{\odot}$ (green points), metal-rich gas with $Z > 10^{-4}\,Z_{\odot}$ (blue points). *Third column*: η distributions for gas (solid line) and dark-matter (dot-dot-dot-dashed line) components; molecular-rich gas with $x_{mol} > 5 \times 10^{-4}$ (red dotted line), metal-rich gas with $Z > 10^{-3}\,Z_{\odot}$ (green dashed line), metal-rich gas with $Z > 10^{-4}\,Z_{\odot}$ (blue dot-dashed line) are also marked. *Fourth column*: corresponding ε distributions for the different gas phases.

and for dark matter as well, marked with solid and dot-dot-dot-dashed black lines, respectively.

As a first example, we select a case where both metal-rich (for both the two thresholds considered) and molecular-rich gas are present. The gaseous components have very different behaviours. Molecular-rich gas shows a more elongated morphology, which is confirmed by a broader distribution of η at values > 0. The presence of rotational motions in the molecular-rich gas is also suggested by the values of ε, in the fourth panel, which are centered around $\varepsilon \sim 0.5$. On the contrary, the η distribution of very metal-rich ($Z > 10^{-3}\,Z_{\odot}$) gas does not show any significant sign of coherent rotation, since for roughly $\sim 90\%$ of the gas $\eta \sim 0$ with scattered peaks at random values. Metal-rich material with $Z > 10^{-4}\,Z_{\odot}$ shows intermediate trends, being slightly affected by molecular evolution. This halo is chosen explicitly to highlight the different behaviour of metal-rich and molecular-rich gas in an isolated halo, that is not subject to tidal interactions with closeby structures. The dynamical

differences in the various phases arise consequently to gas collapse, star formation and feedback mechanisms.

The second halo (middle row in Fig. 13) shows instead the typical case where the circular motion of the molecular gas in the central core is mainly driven by interactions with merging sub-haloes occurring during the mass assembly of the main halo. This leads here to the formation of a tail-like feature in the molecular-rich gas, spinning around the halo center. The peak around $\varepsilon \sim 1$ in the fourth-column is basically due to this motion. The non-stable, non-ordered nature of this rotational pattern is reflected by the increasing η, which reaches values greater than 1 for a significant fraction of molecular-rich gas (middle-row, third-column panel). A very interesting example is provided by the isolated, low-mass halo in the last row of Fig. 13, which has no metal-rich gas, but presents an elongated, disc-like rotating structure in the molecular-rich phase. The gas hosted in this halo has not hosted star formation episodes, yet, and its behaviour is led by molecular runaway collapse. Similarly to the first

example, also this small halo does not show interacting features, leading to the conclusion that the establishment of this rotational pattern is mainly driven by the fairly quiescent contraction process, rather than by external forces.

In general, the η distributions for gas and dark matter show how the two components in the central region of the halos respond differently to environmental effects. In particular, the dark-matter distribution is generally flatter and broader with respect to the gas one, meaning that ordered, rotational patterns do not establish in the velocity field but rather preserve random orbits. Regarding the total gas, its behaviour is mainly led by molecular-rich or poorly enriched material, since these phases dominate the central cooling region.

4.3.3 Evolutionary features: survival and destruction of primordial molecular discs

We analyse here the case of the most massive halo in the sample, for which the establishment of rotational substructures in the gaseous core region is captured during the subsequent phases of the merging process with an in-falling subhalo. We present the results in Fig. 14 (colors and symbols are as in Fig. 13).

This halo formed at redshift $z \sim 20$, when the Universe was $\sim 0.2\,\mathrm{Gyr}$ old, and is followed down to $z \simeq 8.5$. As shown from the Figure, the central core of the halo goes from a more relaxed configuration around redshift $z \sim 13$ (when the age of the Universe was $\sim 0.3\,\mathrm{Gyr}$) to a strongly interacting phase due to the in-fall of a subhalo starting at around redshift ~ 11 and completing at $z \sim 9$ (when the Universe was about $0.5\,\mathrm{Gyr}$ old). The sloshing of the core region has the effect of boosting the rotating motion of the molecular-rich gas especially, as one can see from the shift of the ε distribution, towards values peaked around 1. The establishment of a molecular rotating structure is particularly evident at $z \sim 10$, where the two halo cores are mixing. From the comparison of the maps and distributions at $z \sim 12$ and $z \sim 9$ we infer that the disc-like structure in the molecular-rich gas partially survives over time, since at lower redshifts (e.g. $z \sim 9$) the distribution of ε is still biased towards non-zero values, which means that the molecular-rich gas in the very central region does show a mildly rotating component.

In contrast to the disc-like structures that might arise in the star component of galaxies, gaseous rotational patterns have essentially an *intermittent* nature. Given the collisional essence of gas, such rotational motions are strongly influenced by dynamical interactions, which cause them to establish as well as to be easily disrupted in less than a few $10^7\,\mathrm{yr}$ timescales (see also the following Section 4.3.4 for further discussion). Basically, this demonstrates how the phenomenon is more sensitive to close-by passages of sub-haloes accreted by the main halo during its mass assembly, rather than to the passive evolution during the collapse process (a similar result was found, on larger scales, for the hot gas in simulated galaxy clusters by Biffi et al. 2011, 2013).

This is well emphasized by the case study presented in Fig. 14: the hotter, metal-rich gas, if present as in this case, is more likely subject to environmental influences or feedback effects and no stable rotational patterns form, while the dynamical properties of the molecular-rich gas tend to survive longer. In fact, the blue and green η distributions,

corresponding to the metal-rich gas for the two metallicity thresholds, show no significant alignment. In particular, the high-metallicity ($Z > 10^{-3}\,\mathrm{Z_\odot}$) gas has a noisy distribution (e.g. in the third column, third panel) that reflects also the response of hot, enriched material to merging, sloshing and interacting collisional forces. Indeed, the quasi-totality of metal-rich gas is not found in orbits close to circular, being the distribution peaked at $\varepsilon \sim 0$ at all redshifts, independently of the dynamical status. This is a direct consequence of the feedback from star formation, because of which metals are spread randomly with no preferential direction.

As previously discussed in Section 4.3.2, we remark here that the dark-matter component does not show any strong effect of the gas dynamical interactions in the halo core (see third-column panels in Fig. 14).

4.3.4 Statistical properties of rotational patterns

In order to explore the statistical occurrence of rotational gas patterns that establish in proto-galaxy haloes, we investigate the number of haloes featuring a significant amount of co-rotating gas fraction, as function of redshift.

More in detail, we adopt the following procedure:
(i) we compute ε and $\cos\vartheta$ for each particle in each object;
(ii) we calculate the fraction of gas particles with ε, or $\cos\vartheta$, above a significant threshold, $f_{\varepsilon > \varepsilon_{\mathrm{th}}}$ and $f_{\cos\vartheta > \cos\vartheta_{\mathrm{th}}}$;
(iii) we require a halo to contain at least 20% of co-rotating gas particles – as additional check, we repeat this last part of the analysis with the stricter requirement of at least 50% of co-rotating gas particles.

For sake of clarity, we consider as *co-rotating gas particles* those with either $\varepsilon > 0.5$ or $\cos\vartheta > 0.8$, and explore first the two cases separately. In fact, the two thresholds chosen, $\varepsilon_{\mathrm{th}} = 0.5$ and $\cos\vartheta_{\mathrm{th}} = 0.8$ (i.e. $\theta_{\mathrm{th}} \simeq 37^o$), represent reasonable values comprised among the cases investigated in the parameter study (see also Appendix A)

We stress that, by construction, the majority of the haloes, independently of the parameters used to quantify the rotating fraction of the gas (either ε or $\cos\vartheta$) as well as of redshift and of molecular or metal content, show prevalently co-rotating features (namely, positive alignment). Barely for a handful of haloes, the $\cos\vartheta$ diagnostics points out a contra-rotating gas fraction ($f_{\cos\vartheta < -\cos\vartheta_{\mathrm{th}}}$) up to $\sim 10 - 25\%$ (see Fig. 19, top-row panels). For this reasons, we concentrate the following statistical analysis on co-rotating gas, only.

In Fig. 15 we report the fraction of haloes featuring more than 20% (solid curves; or 50%, dashed curves) of co-rotating gas, as a function of redshift. In each panel we show the trends for molecular-rich gas (red histograms) and metal-rich gas above the two metallicity thresholds (green for gas with $Z > 10^{-3}\,\mathrm{Z_\odot}$ and blue for gas with $Z > 10^{-4}\,\mathrm{Z_\odot}$), separately.

In the left panel of Fig. 15 we show the results of the $\cos\vartheta$ diagnostics. Since this is the weaker indicator of potential rotation of the two analysed so far ($\cos\vartheta$ and ε), it allows us to single out, on average, more candidates for halos hosting gas rotational motions. In fact, when the co-rotating gas is defined by requiring $\cos\vartheta > 0.8$, we find a fairly large fraction of haloes with at least 20% co-rotating molecular-rich gas, ranging from 2% at $z \sim 19$ up to $\sim 12\%$ at $z \lesssim 10$. A non-negligible fraction of haloes (from a few per cent at $z \sim 15$ up to $6 - 8\%$ at $z \sim 9$) also shows rotational features
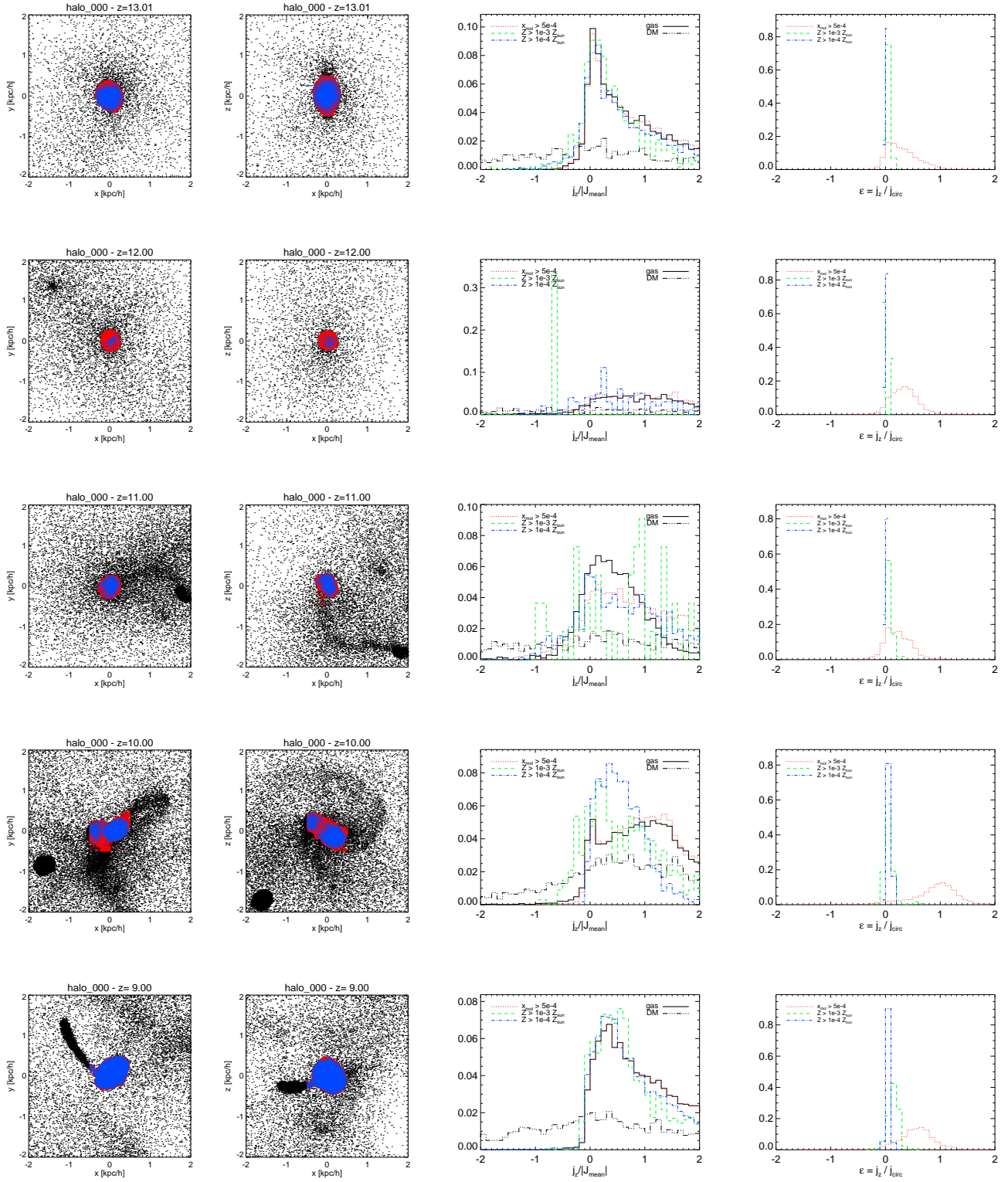
Figure 14. Evolution with redshift of the biggest halo in the sample. The establishment and enhancement of rotational patterns in the molecular-rich gas of the halo is captured while the halo is merging with an in-falling sub-halo. The snapshots refer to redshift $z = 13.01$ (first row), 12.00 (second row), 11.00 (third row), 10.00 (fourth row) and 9.00 (fifth row), when the corresponding age of the Universe was about 323, 361, 407, 464 and 535 Myr (in the standard ΛCDM model). For the quantities plotted in the columns and color code, we refer to Fig. 13.
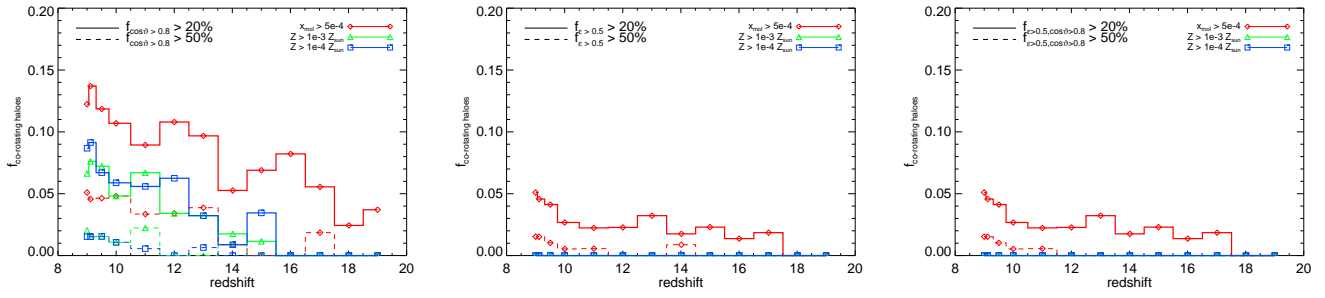
Figure 15. Redshift evolution for the fraction of haloes hosting a significant percentage of co-rotating gas ($> 20\%$, solid; $> 50\%$, dashed), for the different gas phases considered, as in the legend (see also text and previous figures). Different panels refer to the different diagnostics used to identify co-rotating gas: $\cos\vartheta > 0.8$ (left), $\varepsilon > 0.5$ (center), and both indicators combined, i.e. $\cos\vartheta > 0.8$ *and* $\varepsilon > 0.5$ (right).

when the metal-rich gas phase is considered. Lower fractions (by a factor of roughly 2-3), but similar trends with redshift, are found when we consider only haloes with a minimum of 50% co-rotating gas.

The ε diagnostics (Fig. 15, middle panel) provides more stringent, quantitative estimates of the number of haloes containing a non-negligible fraction of gaseous rotational patterns. This presents a qualitatively similar, but quantitatively different picture with respect to the previous case. On average, in a few per cent of the haloes between $z \sim 9$ and $z \sim 19$, at least 20% of the molecular-rich gas is co-rotating. At $z \sim 18$ the initial fraction of haloes hosting co-rotating gas is $\sim 2\%$ and at $z \sim 9$ this fraction reaches $\sim 5\%$. If one restricts further the definition of disc and considers only haloes hosting at least 50% of molecular-rich, co-rotating gas, then it turns out that barely $1 - 2\%$ of early objects contain primordial molecular discs at $z \lesssim 14$.

As anticipated from the previous single case studies (Section 4.3.2 and Section 4.3.3), the results from the ε diagnostics in Fig. 15 also confirm that, statistically, metal-rich gas does not feature rotational patterns. Indeed, the metal-rich gas is hotter than the molecular-rich gas, which makes its collisional nature to be significantly more important in preventing disc-like structures to establish and, especially, to survive long enough against tidal disruption and environmental effects. Because of its colder temperatures, typically $\lesssim 10^4$K, the molecular-rich component is instead less strongly affected. In fact, even in the case when the formation of a rotational pattern in the molecular-rich gas is temporarily driven by dynamical interactions, it still survives in time and does not dissolve entirely as quickly as in the metal-rich gas case (see Fig. 14, and previous discussion in Section 4.3.3).

For a final, more robust verification, we make a more stringent requirement by defining *co-rotating gas particles* those with both $\varepsilon > 0.5$ *and* $\cos\vartheta > 0.8$. The combination of the two methods (Fig. 15, right panel) basically mirrors the ε diagnostics, which in fact points out rotational patterns in a more reliable way. The only difference between middle and right panels consists of one single halo at $z \sim 14$, for which more than 50% of the molecular-rich gas has $\varepsilon > 0.5$ but the alignment angle ϑ is larger than $\sim 37^o$ (i.e. $\cos\vartheta < 0.8$). When the required fraction of rotating gas is 20%, absolutely no difference is found.
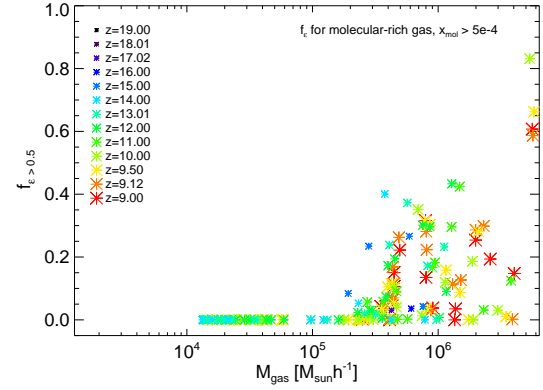

Figure 16. Fraction of the molecular-rich gas in each halo with $\varepsilon > 0.5$ as a function of the halo gas mass. Different colors and symbol sizes refer to the redshifts analysed, as in the legend. The correlation coefficient between $f_{\varepsilon>0.5}$ and M_{gas} is ~ 0.65. When we consider M_{DM} or $M_\star$, instead of M_{gas}, similar behaviours are recovered with correlation coefficients of ~ 0.59 and ~ 0.41, respectively.

4.3.5 Establishment of rotational patterns: correlation with the hosting mass

The fraction of haloes for which the molecular-rich gas shows significant co-rotating patterns could also depend on the hosting mass. This possibility is studied in Fig. 16, where the fraction of molecular-rich gas with $\varepsilon > 0.5$, $f_{\varepsilon>0.5}$, is plotted as a function of the halo gas mass. We focus, to this purpose, on the ε diagnostic solely, being this the most reliable indicator of rotational motions. We note that on average $f_{\varepsilon>0.5}$ increases with the mass of the gas in the halo, quite independently of the redshift considered, but with a large spread. Objects with low masses ($M_{gas} \lesssim 2 \times 10^5$ M$_\odot/h$) present a fraction of co-rotating, molecular-rich gas which is extremely low, basically zero, because they have not formed enough molecules to cool and condense in a disc-like structure, yet. Such mass limit is consistent with the minimum dark-matter mass of $M_{DM} \sim 2 \times 10^6$ M$_\odot/h$ needed to host runaway gas collapse and star formation (as discussed in Section 4 and 3, and demonstrated in Fig. 1). Slightly larger objects instead have a fraction of rotating, molecular-rich gas, $f_{\varepsilon>0.5}$, that ranges between $\sim 20\%$ and $\sim 60\%$ de-
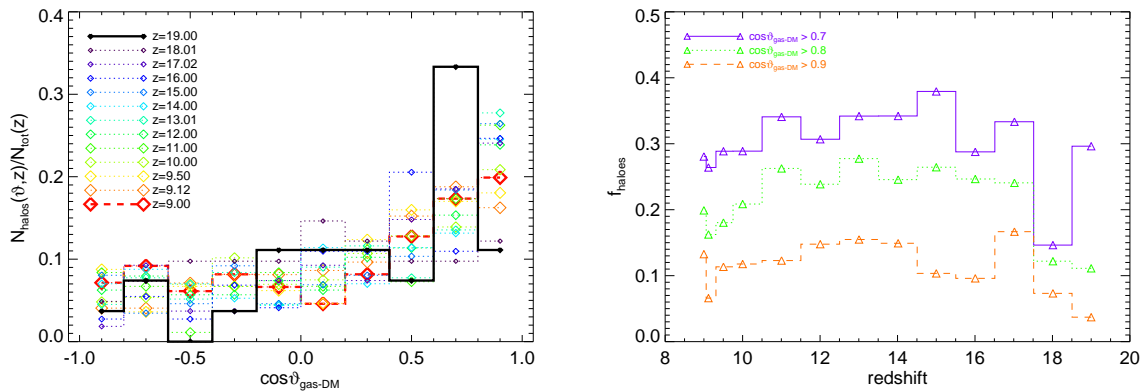
Figure 17. *Left panel:* fraction of haloes, at each redshift, with a certain degree of alignment between the gaseous core and the large-scale dark-matter component, quantified by the cosine of the angle formed by their mean angular momenta, plotted on the x-axis; we mark with thicker lines the first ($z = 19$) and last ($z = 9$) redshift considered. *Right panel:* distribution with redshift of the fraction of haloes for which $cos\vartheta_{\mathrm{gas-DM}}$ is greater than 0.7 (solid purple line), 0.8 (dotted green line), 0.9 (dashed orange line).

pending also on the local environments. For the larger and more evolved proto-galaxies with $M_{gas} \sim 10^7$ M$_\odot/h$ and $M_{DM} \sim 10^8$ M$_\odot/h$, $f_{\varepsilon > 0.5}$ can easily exceed 60% and reach $\sim 85\%$. The dependence of rotating, molecular gas on the hosting gas, dark-matter or stellar mass is quantified by the Pearson correlation coefficient between $f_{\varepsilon > 0.5}$ and M_{gas}, M_{DM} or $M_\star$. The resulting values turn out to be ~ 0.65, ~ 0.59 and ~ 0.41, respectively. Thus, we conclude that the establishment of gaseous rotational patterns in the innermost regions of early objects is mildly related to the whole hosting mass. In particular, the null values at law masses and the higher values at larger masses suggest the importance of overcoming the mass threshold for gas cooling and collapse. The broad spread for $M_{gas} \gtrsim 2 \times 10^5$ M$_\odot/h$ (i.e. $M_{DM} \gtrsim 2 \times 10^6$ M$_\odot/h$) is a consequence of the backreaction of feedback mechanisms on the following gas evolution.

4.3.6 Angular momentum alignment of gas and dark-matter components

As a further issue, we explore the global alignment between the mean angular momentum of the gas in the core region and the one of the whole dark-matter distribution. In this way we will gain hints on the dynamical effects of the large-scale dark-matter component on the innermost gaseous core, where the first events of baryonic structure formation take place, the majority of molecular- and metal-rich gas resides and the disc-like patterns are likely to establish.
In particular, we investigate the statistical distributions for $cos\vartheta_{\mathrm{gas-DM}}$ at different z (Fig. 17) and the resulting correlation to the hosting mass (Fig. 18).
The left panel of Fig. 17 shows a slightly increasing trend of the distribution at $cos\vartheta_{\mathrm{gas-DM}} \gtrsim 0.5$ and therefore give support for a mild alignment of gas and dark-matter components mostly at high redshifts.
The right panel of the Figure reports the fraction of haloes with prominent alignment (i.e. $cos\vartheta_{\mathrm{gas-DM}} > 0.9$) between the central gas and the large-scale dark-matter halo, as a function of redshift. We note that this fraction increases from redshift $z \sim 20$ up to $z \sim 14$, meaning that the large-scale dark-matter halo has a mild effect on the central gas,

building some alignment during the early stages of the collapse process and mainly reflecting the ongoing star formation activity, afterwards. At redshift $z \lesssim 14$, we find maximum alignment for about $\sim 10\%$ of the haloes, for which $cos\vartheta_{\mathrm{gas-DM}} > 0.9$ (i.e. $\vartheta_{\mathrm{gas-DM}} \lesssim 26^o$). Similar results are recovered also when less stringent alignment criteria are applied (namely, $\vartheta_{\mathrm{gas-DM}} \lesssim 37^o, 45^o$), by which the fraction of haloes satisfying them naturally increases at all redshifts, reaching $\sim 20 - 30\%$ at $z \sim 9$. The general, mild drop at later times is simply interpreted as a consequence of the more chaotic environment established after first star formation episodes and SN explosions.
To check whether the alignments are related to the hosting mass, in Fig. 18 we plot the cosine of the angle formed by the angular momentum vectors of the (central) gas and dark-matter components as a function of mass, for all the haloes and at all the redshifts considered. As a result, we find no evidence for dependence on the hosting mass of the alignment ($cos\vartheta_{\mathrm{gas-DM}}$). In a more quantitative way, the Pearson correlation coefficient is very small, both by considering all the redshifts together (~ -0.03) and by considering individual redshift bins (ranging from ~ -0.09 to 0.13). The same conclusion is found when investigating correlation between $cos\vartheta_{\mathrm{gas-DM}}$ and M_{DM}, for which the correlation coefficient is only ~ -0.04.

5 CONCLUSIONS

In the previous sections we have investigated baryonic and dynamical features of the first proto-galaxies by analyses of numerical hydrodynamical simulations including atomic and molecular chemistry (following e^-, H, H$^+$, H$^-$, He, He$^+$, He^{++} D, D$^+$, H$_2$, H$_2^+$, HD, HeH$^+$), cooling, star formation and self-consistent stellar evolution according to proper yields (for He, C, O, Si, Fe, Mg, S, etc.) and lifetimes for popIII and popII-I regimes (as outlined also in Section 2). To this purpose, we have analysed a significantly large sample of early proto-haloes (1680 objects) all very well resolved with at least 300 gas particles (Section 3), at redshift $\gtrsim 9$. First galaxies form in small H$_2$-cooling haloes with gas
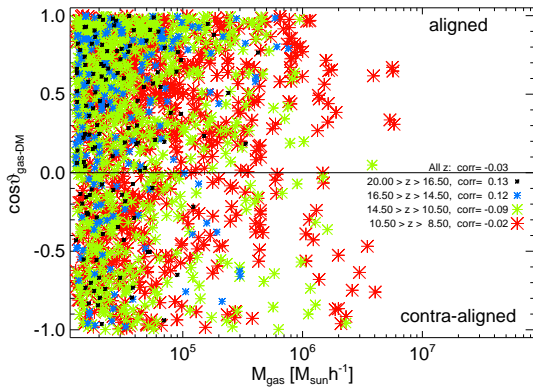
Figure 18. Relation between the alignment of central gas and large-scale dark-matter angular momentum and the halo gas mass. As explained by the labels, four bins in redshift are considered separately. Values of $cos\vartheta_{gas-DM} = 1, -1$ represent maximum alignment and contra-alignment, respectively. The correlation coefficient is close to zero, both for the individual redshift bins and considering all the points together.

masses $\sim 10^5 - 10^7$ M$_\odot$ and stellar fractions $\lesssim 10^{-3}$ (Fig. 1), broadly dispersed and with properties severely affected by environmental effects (e.g. Fig. 4).

The minimum mass for star formation is found to be $M_{DM} \sim 2 \times 10^6$ M$_\odot$, as gas in smaller structures does not reach densities high enough to trigger significant molecule creation, cooling and fragmentation of the medium (Fig. 5). Early popIII galaxies are relevant in polluting the surrounding medium up to $\sim 10^{-2}$ Z$_\odot$ during the very first bursts (Fig. 2). In total, roughly $\lesssim 10$ per cent of the objects by $z \sim 9$ is enriched above the critical popII-I threshold,

UM:

but contribute to more than ~ 80 per cent of the halo SFR (Fig. 3). This suggests that pristine or weakly polluted (quiescent) proto-galaxies might well exist at lower z (as argued in Maio et al. 2013, too).

Furthermore, among the polluted structures, roughly $\sim 60\%$ are actively forming stars, the remaining quiescent $\sim 40\%$ being usually enriched by nearby sources (Section 4.1.1).

PopIII and popII-I stellar evolution is responsible for enriching completely closeby, low-mass, non-star-forming galaxies with hot material that experienced feedback in relatively larger, more active galaxies. This is the case for roughly ~ 7 per cent of the enriched-halo sample at $z \gtrsim 9$. None the less, the majority of the polluted haloes (roughly 93%) shows signature of both external and *in situ* enrichment (see Table 1). Feedback mechanisms alter their abundances and determine a significant spread (of up to ~ 2 orders of magnitude) when looking at the different correlations involving gas masses, temperatures, local star formation rates, or chemical composition, as x_{mol} and Z (Fig. 6 and Fig. 8). Their impact is less important for haloes that evolve in isolation or far away from the main star formation sites, though.

As a consequence of molecular-driven star formation and metal pollution, relations between stellar mass, SFR and metallicity are expected (Fig. 9), but outliers can persist due to environmental dependencies.

A fundamental link to understand early star formation lies in the **roughly linear $x_{mol} - f_\star$** relation (Fig. 10), while

large scatter for Z values in similar mass (or SFR) bins can be simply determined by the effects of metal spreading in denser or rarer regions.

Typical star formation rates are around SFR $\sim 10^{-7} - 10^{-3}$ M$_\odot$/yr, corresponding to mean specific values of sSFR ~ 10 Gyr^{-1} at $z \sim 9$ and ~ 50 Gyr^{-1} at $z \sim 10 - 20$. For individual primordial cases, sSFRs of the order of $\sim 10^2$ Gyr^{-1} at can be reached, as well (Fig. 11). These values make primordial galaxies very bursty objects (Fig. 12) .

Gaseous rotational features are quantified through the analysis of the gas specific angular momentum. We find that the establishment of strong rotationally-supported gaseous cores in early proto-galaxies is not very common, in agreement with recent studies by Prieto et al. (2013), but based on a larger sample (which significantly increased the statistics) of numerical, hydro, chemistry simulations, including star formation, stellar evolution, metal production and feedback processes.

Additionally, we note that gaseous rotational patterns generally evolve in an intermittent fashion and show striking differences for different gas phases: the molecular-rich component tends to maintain any established rotational motion longer with respect to the hotter, metal-rich gas phase, which is more sensitive to the environment (sub-haloes infall, star formation bursts, feedback processes, mergers) and thus shows a more chaotic nature (Fig. 13 and Fig. 14).

In general, the establishment of such gas rotational motions in the halo innermost region is found to be mildly dependent on the whole hosting mass, with $\gtrsim 60\%$ of molecular-rich gas featuring rotation in haloes larger than $M_{gas} > 10^6$ M$_\odot$/h and $M_{DM} > 10^7$ M$_\odot$/h (Fig. 16). Moreover, the fraction of objects with a significant amount of co-rotating molecular-rich gas increases in time from a few per cent at $z \sim 18$ up to $\sim 5 - 15$ per cent at $z \lesssim 10$ (Fig. 15).

With our analysis we also observe that the (mis-)alignment between gas and dark-matter angular momenta does not indicate a significant dependence on the halo mass (Fig. 18). On the other hand, a certain mild trend in redshift appears (Fig. 17), with the fraction of haloes that show maximum spin alignments increasing from $1 - 2$ per cent at $z \sim 19$ and reaching $\sim 10\%$ at redshift $z \sim 9$.

We stress that we checked our conclusions by applying different resolution requirements for each halo (as specified in Section 3), however, all the resulting trends did not show evident changes and the statistical patterns were basically unaffected.

Figure 19. Fractional distributions $f_{cos\vartheta}$ (upper row) and f_ε (lower row) as a function of redshift. Columns refer to the gas phase considered, namely: molecular-rich gas with $x_{mol} > 5 \times 10^{-4}$ (left); metal-rich gas with $Z > 10^{-3}$ $Z_\odot$ (middle); metal-rich gas with $Z > 10^{-4}$ $Z_\odot$. In every panel, each halo is marked with two points, representing the fraction of co-rotating (red diamonds) or contra-rotating (black triangles) gas (see legend and text).

REFERENCES

Abel T., Bryan G. L., Norman M. L., 2002, Science, 295, 93

Alvarez M. A., Wise J. H., Abel T., 2009, ApJ, 701, L133

Bate M. R., Burkert A., 1997, MNRAS, 288, 1060

Biffi V., Dolag K., Böhringer H., 2011, MNRAS, 413, 573

Biffi V., Dolag K., Böhringer H., 2013, MNRAS, 428, 1395

Binney J., Tremaine S., 2008, Galactic Dynamics: Second Edition. Princeton University Press

Bouwens R., Bradley L., Zitrin A., and 35 co-authors, 2012, ArXiv e-prints

Bower R. G., Vernon I., Goldstein M., Benson A. J., Lacey C. G., Baugh C. M., Cole S., Frenk C. S., 2010, MNRAS, 407, 2017

Brinchmann J., Charlot S., White S. D. M., Tremonti C., Kauffmann G., Heckman T., Brinkmann J., 2004, MNRAS, 351, 1151

Bromm V., Loeb A., 2003a, ApJ, 596, 34

Bromm V., Loeb A., 2003b, Nature, 425, 812

Brooks A. M., Governato F., Quinn T., Brook C. B., Wadsley J., 2009, ApJ, 694, 396

Campisi M. A., Maio U., Salvaterra R., Ciardi B., 2011, MNRAS, 416, 2760

Coe D., Zitrin A., Carrasco M., Shu X., Zheng W., 18 co-authors 2013, ApJ, 762, 32

Cooray A., Bock J. J., Keatin B., Lange A. E., Matsumoto T., 2004, ApJ, 606, 611

Creasey P., Theuns T., Bower R. G., 2012, ArXiv e-prints

Daddi E., Dickinson M., Morrison G., Chary R., Cimatti A., Elbaz D., Frayer D., Renzini A., Pope A., Alexander D. M., Bauer F. E., Giavalisco M., Huynh M., Kurk J., Mignoli M., 2007, ApJ, 670, 156

Davé R., Oppenheimer B. D., Finlator K., 2011, MNRAS, 415, 11

Dayal P., Dunlop J. S., Maio U., Ciardi B., 2013, MNRAS

de Souza R. S., Ciardi B., Maio U., Ferrara A., 2013, MNRAS, 428, 2109

Dekel A., Birnboim Y., Engel G., Freundlich J., Goerdt T., Mumcuoglu M., Neistein E., Pichon C., Teyssier R., Zinger E., 2009, Nature, 457, 451

Dolag K., Borgani S., Murante G., Springel V., 2009, MNRAS, 399, 497

Dunlop J. S., Rogers A. B., McLure R. J., 16 co-authors 2013, MNRAS, 432, 3520

Dwek E., Arendt R. G., 1998, ApJ, 508, L9

Elbaz D., Daddi E., Le Borgne D., Dickinson M., Alexander D. M., Chary R.-R., Starck J.-L., Brandt W. N., Kitzbichler M., MacDonald E., Nonino M., Popesso P., Stern D., Vanzella E., 2007, A&A, 468, 33

Fernandez E. R., Shull J. M., 2011, ApJ, 731, 20

Fernandez E. R., Zaroubi S., 2013, ArXiv e-prints

Fialkov A., Barkana R., Tseliakhovich D., Hirata C. M., 2012, MNRAS, 424, 1335

Genzel R., Burkert A., Bouché N., Cresci G., Förster Schreiber N. M., Shapley A., Shapiro K., Tacconi L. J., 17 co-authors 2008, ApJ, 687, 59

González V., Bouwens R. J., Labbé I., Illingworth G., Oesch P., Franx M., Magee D., 2012, ApJ, 755, 148

Gorjian V., Wright E. L., Chary R. R., 2000, ApJ, 536, 550

Greif T. H., Johnson J. L., Klessen R. S., Bromm V., 2008, MNRAS, 387, 1021

Greif T. H., White S. D. M., Klessen R. S., Springel V., 2011, ApJ, 736, 147

Gunn J. E., Gott III J. R., 1972, ApJ, 176, 1

Halle A., Combes F., 2012, ArXiv e-prints

Jeeson-Daniel A., Ciardi B., Maio U., Pierleoni M., Dijkstra M., Maselli A., 2012, MNRAS, 424, 2193

Jeeson-Daniel A., Dalla Vecchia C., Haas M. R., Schaye J., 2011, MNRAS, 415, L69

Johnson J. L., Whalen D. J., Fryer C. L., Li H., 2012, ApJ, 750, 66

Karim A., Schinnerer E., Martínez-Sansigre A., Sargent M. T., van der Wel A., Rix H.-W., Ilbert O., Smolčić V., Carilli C., Pannella M., Koekemoer A. M., Bell E. F., Salvato M., 2011, ApJ, 730, 61

Kashlinsky A., 2005, ApJ, 633, L5

Kashlinsky A., Arendt R. G., Ashby M. L. N., Fazio G. G., Mather J., Moseley S. H., 2012, ApJ, 753, 63

Kennicutt Jr. R. C., 1998, ApJ, 498, 541

Kereš D., Katz N., Weinberg D. H., Davé R., 2005, MNRAS, 363, 2

Labbé I., González V., Bouwens R. J., Illingworth G. D., Franx M., Trenti M., Oesch P. A., van Dokkum P. G., Stiavelli M., Carollo C. M., Kriek M., Magee D., 2010, ApJ, 716, L103

Madau P., Rees M. J., 2001, ApJ, 551, L27

Magliocchetti M., Salvaterra R., Ferrara A., 2003, MNRAS, 342, L25

Maio U., 2011a, Classical and Quantum Gravity, 28, 225015

Maio U., 2011b, Classical and Quantum Gravity, 28, 225015

Maio U., Ciardi B., Dolag K., Tornatore L., Khochfar S., 2010, MNRAS, 407, 1003

Maio U., Ciardi B., Mueller V., 2013, ArXiv e-prints

Maio U., Dolag K., Ciardi B., Tornatore L., 2007, MNRAS, 379, 963

Maio U., Dolag K., Meneghetti M., Moscardini L., Yoshida N., Baccigalupi C., Bartelmann M., Perrotta F., 2006, MNRAS, 373, 869

Maio U., Dotti M., Petkova M., Perego A., Volonteri M., 2013, ApJ, 767, 37

Maio U., Iannuzzi F., 2011, MNRAS, 415, 3021

Maio U., Khochfar S., 2012, MNRAS, 421, 1113

Maio U., Khochfar S., Johnson J. L., Ciardi B., 2011, MNRAS, 414, 1145

Maio U., Koopmans L. V. E., Ciardi B., 2011, MNRAS, 412, L40

Maio U., Salvaterra R., Moscardini L., Ciardi B., 2012, MNRAS, 426, 2078

Mannucci F., Cresci G., Maiolino R., Marconi A., Gnerucci A., 2010, MNRAS, 408, 2115

McQuinn M., O'Leary R. M., 2012, ApJ, 760, 3

Michałowski M., Hjorth J., Watson D., 2010, A&A, 514, A67

Moster B. P., Macciò A. V., Somerville R. S., Naab T., Cox T. J., 2012, MNRAS, 423, 2045

Naoz S., Yoshida N., Gnedin N. Y., 2012, ApJ, 747, 128

Naoz S., Yoshida N., Gnedin N. Y., 2013, ApJ, 763, 27

Noeske K. G., Weiner B. J., Faber S. M., Papovich C., Koo D. C., Somerville R. S., 23 co-authors 2007, ApJ, 660, L43

Pannella M., Carilli C. L., Daddi E., McCracken H. J., Owen F. N., Renzini A., Strazzullo V., 13 co-authors 2009, ApJ, 698, L116

Peng Y.-j., Lilly S. J., Kovač K., 61 co-authors 2010, ApJ, 721, 193

Petkova M., Maio U., 2012, MNRAS, 422, 3067

Petkova M., Springel V., 2011, MNRAS, 412, 935

Piontek F., Steinmetz M., 2011, MNRAS, 410, 2625

Prieto J., Jimenez R., Haiman Z., 2013, ArXiv e-prints

Reddy N. A., Pettini M., Steidel C. C., Shapley A. E., Erb D. K., Law D. R., 2012, ApJ, 754, 25

Richardson M. L. A., Scannapieco E., Thacker R. J., 2013, ArXiv e-prints

Ricotti M., Gnedin N. Y., Shull J. M., 2001, ApJ, 560, 580

Robertson B. E., Ellis R. S., Dunlop J. S., McLure R. J., Stark D. P., 2010, Nature, 468, 49

Rodighiero G., Daddi E., 32 co-authors 2011, ApJ, 739, L40

Romano-Díaz E., Choi J.-H., Shlosman I., Trenti M., 2011, ApJ, 738, L19

Sales L. V., Navarro J. F., Theuns T., Schaye J., White S. D. M., Frenk C. S., Crain R. A., Dalla Vecchia C., 2012, MNRAS, 423, 1544

Salim S., Rich R. M., Charlot S., 21 co-authors 2007, ApJS, 173, 267

Salvaterra R., Ferrara A., Dayal P., 2011, MNRAS, 414, 847

Salvaterra R., Maio U., Ciardi B., Campisi M. A., 2013, MNRAS, 429, 2718

Santos M. R., Bromm V., Kamionkowski M., 2002, MNRAS, 336, 1082

Schmidt M., 1959, ApJ, 2129, 243

Schneider R., Ferrara A., Salvaterra R., Omukai K., Bromm V., 2003, Nature, 422, 869

Skibba R. A., Macciò A. V., 2011, MNRAS, 416, 2388

Sokasian A., Yoshida N., Abel T., Hernquist L., Springel V., 2004, MNRAS, 350, 47

Springel V., Hernquist L., 2003, MNRAS, 339, 289

Stacy A., Bromm V., 2013, ArXiv e-prints

Stacy A., Bromm V., Loeb A., 2011, ApJ, 730, L1

Stacy A., Greif T. H., Klessen R. S., Bromm V., Loeb A., 2013, MNRAS, 431, 1470

Stark D. P., Schenker M. A., Ellis R., Robertson B., McLure R., Dunlop J., 2013, ApJ, 763, 129

Toomre A., 1977, ARA&A, 15, 437

Tornatore L., Borgani S., Viel M., Springel V., 2010, MNRAS, 402, 1911

Tornatore L., Ferrara A., Schneider R., 2007, MNRAS, 382, 945

Totani T., Yoshii Y., Maihara T., Iwamuro F., Motohara K., 2001, ApJ, 559, 592

Tremonti C. A., Heckman T. M., Kauffmann G., Brinchmann J., Charlot S., White S. D. M., Seibert M., Peng E. W., Schlegel D. J., Uomoto A., Fukugita M., Brinkmann J., 2004, ApJ, 613, 898

Tseliakhovich D., Hirata C., 2010, Phys. Rev. D, 82, 083520

Vazza F., Dolag K., Ryu D., Brunetti G., Gheller C., Kang H., Pfrommer C., 2011, MNRAS, 418, 960

Vogelsberger M., Genel S., Sijacki D., Torrey P., Springel V., Hernquist L., 2013, ArXiv e-prints

Whalen D., O'Shea B. W., Smidt J., Norman M. L., 2008, ApJ, 679, 925

White S. D. M., Rees M. J., 1978, MNRAS, 183, 341

Wise J. H., Abel T., 2007, ApJ, 665, 899

Wise J. H., Turk M. J., Norman M. L., Abel T., 2012, ApJ, 745, 50

Xu H., Wise J. H., Norman M. L., 2013, ArXiv e-prints

Yoshida N., Abel T., Hernquist L., Sugiyama N., 2003, ApJ, 592, 645

Zheng W., Postman M., Zitrin A., 33 co-authros 2012, Nature, 489, 406

APPENDIX A: PARAMETER STUDY

We present here some demonstration cases of the parameter study done to ascertain the reliability of the conclusions drawn, independently of the assumptions made for the calculations. More precisely, we have studied parameter dependences for the fractional distributions $f_{\cos\vartheta}$ and f_ε, i.e. the fractions of gas with $\cos\vartheta > |\cos\vartheta_{\rm th}|$ and $\varepsilon > |\varepsilon_{\rm th}|$, respectively.

First, we find that the trends are not significantly sensitive to the precise sampling of the central regions, for 1.00, 0.50, and 0.25 kpc/h comoving radii. In fact, since we aim at studying rotational patterns in the molecular-rich and metal-rich gas, the selected gaseous components mainly reside, in any case, in the very central sites of the halo, so that no striking difference is introduced by the exact core size. Moreover, the results on rotational patterns do not show any strong dependence on the threshold angle $\vartheta_{\rm th}$, used to point out the fraction of aligned, potentially rotating gas, as long as $\cos\vartheta_{\rm th} \gtrsim 0.7$. To ascertain this, the values explored as minimum threshold for the inclination angle are

- $\cos\vartheta_{\rm th} = 0.7$, corresponding to $\theta_{\rm th} \simeq 45^o$,
- $\cos\vartheta_{\rm th} = 0.8$, corresponding to $\theta_{\rm th} \simeq 37^o$,
- $\cos\vartheta_{\rm th} = 0.9$, corresponding to $\theta_{\rm th} \simeq 26^o$.

Given the strong similarity of the results with varying parameters, in Fig. 19 we only show the reference cases (used in the computations for the previous sections), for which the size of the core region is assumed to be 0.5 kpc/h and the minimum threshold angle is $\theta_{\rm th} \simeq 37^o$. The figure displays the fractional distributions f_ε and $f_{cos\vartheta}$ as a function of redshift, for molecular gas ($x_{mol} > 5 \times 10^{-4}$; left column) and metal-rich gas with $Z_{\rm crit} = 10^{-3}\,Z_\odot$ (middle column) and $Z_{\rm crit} = 10^{-4}\,Z_\odot$ (right column). In the plots, each halo is marked with two points, representing the fraction $f_{cos\vartheta}$ of gas for which $\cos\vartheta$ is $> \cos\vartheta_{\rm th}$ (red diamond; co-rotating fraction) and $< -\cos\vartheta_{\rm th}$ (black triangle; contra-rotating fraction), respectively (upper-row panels of Fig. 19). The same is done for f_ε (lower-row panels).

As already highlighted by the representative haloes discussed in Section 4.3.2 and Section 4.3.3, even this statistical analysis confirms that for metal-rich gas, no significant alignment is found between gas particle angular momentum and the circular reference value, j_{circ}. Moreover, this result does not depend on the core size, since the f_ε distribution is always found to be flat around zero at all redshifts, as in the central and right panels of the lower row of Fig. 19. Basically, this indicates that on average there is no evidence of ordered, rotational patterns in the metal-rich gas component. This parameter study also reasserts that a different case is represented by the molecular-rich gas, for which a significant number of haloes, increasing with cosmic time, shows a large gas fraction with co-rotating features, as indicated not only from the $\cos\vartheta$ diagnostics (upper row panels) but also via the more robust ε indicator (lower row panels).